Universiteit Utrecht

IMAU
Institute for Marine and Atmospheric research Utrecht

Faculteit Bètawetenschappen
Faculteit Geowetenschappen

Hydrodynamical and morphological evolution of an open channel under tidal forcing

Bachelor Thesis

Jochem Veerman

Natuur- en Sterrenkunde en Aardwetenschappen

Supervisors:

Prof. Dr. H.E. (Huib) de Swart
Institute for Marine and Atmospheric research Utrecht (IMAU)

Dr. M. (Maarten) van der Vegt
Institute for Marine and Atmospheric research Utrecht (IMAU)

June 16, 2021

Abstract

The future of the Wadden Sea is uncertain, due to the accelerated sea level rise back-barrier systems, like those of the Wadden Sea might drown in the future. The focus in this study is of gaining fundamental understanding on the hydrodynamical and morphological processes of basins that are connected to two different inlets. To do so, a double-inlet basin is schematised as a one-dimensional straight channel with two entrances. The Marsdiep-Vlie channel in the western part of the Dutch Wadden Sea is selected as a prototype, where the incoming wave is a M2 tide. By imposing an incoming M2 tidal wave on both entrances (with a possible phase/amplitude shift between them) and by assuming the hydrodynamics to be weakly non-linear, approximate solutions are obtained for the water motion, sediment transport rate and evolution of the basin (in terms of length and depth). For the evolution of the channel, two cases are studied. First is the symmetrical case, where the incoming tidal wave at both entrances does not have a phase and amplitude shift. Second is the asymmetrical case, where such a phase and amplitude shift does occur. It is found that without sea level rise, the basins in the symmetrical case either fills up (short basins) or tends towards a stable equilibrium. For the non-symmetrical case, export is dominant resulting in deepening and lengthening of the basin. When the current-day sea level rise is added, most initially long and deep basins drown, whereas short, shallow basins fill up for the symmetrical case. In the non-symmetrical case, the deepening and lengthening of the basin is accelerated and initially short, shallow basins increase in size. Similar behaviour is found when using the sea level rise of the RCP2.6 scenario of the IPCC.

The cover image shows the author and his brother running dry with a sailboat on a sand bank of the Wadden Sea near the island of Schiermonnikoog.

Plain English summary

The Wadden Sea is an UNESCO World heritage site in the northern part of the Netherlands and is important for the economy of that region. However, due to climate change and the accompanied accelerated sea level rise, the future of the Wadden Sea becomes uncertain. When the sea level rises too fast, this area with its landscape of tidal flats and channels might drown in the future. The Wadden sea consists of tidal inlets (the gaps between the islands). These inlets are often connected with each other by channels, for example between the Marsdiep-Vlie channel between the Marsdiep and Vlie inlets. The currents, which are primarily generated by tides, are dependent on, among other things, the depth and length of the inlet. When due to sea level rise the depth changes, also the current changes. Since the moving water causes sand to move, the transport of sand changes. As a result, the length and depth of the inlet change.

In this study, a double tidal inlet system is studied. Such a system is schematised as a straight one-dimensional channel with two entrances on opposite side, to gain insight into the physical mechanisms that determine the future of the Wadden Sea. Here, the channel between the Marsdiep and Vlie inlet is used as a prototype. However the theory can be applied more generically to any double tidal inlet system. In this study, two cases are studied. First is the symmetric case, for which the incoming tidal wave at both entrances have equal magnitude and the floods/ebbs occur at the same time. The second is the asymmetric case, where a magnitude and difference in timing of the ebbs/floods is present. The latter case mimics the Marsdiep-Vlie channel.

When the time-evolution of the channel mimicking the Marsdiep-Vlie channel is considered, this model shows that under the sea level rise occurring today, the channel first becomes shorter and shallow, after which it increases in size. When the RCP2.6 scenario of the IPCC is considered (strictest policy), the channel drowns according to this model. This model can be used to study physical mechanisms of the tides in such a channel, but not to obtain the most realistic evolution possible.

Contents

1 Introduction

Barrier islands are found around the world and form a major part of the coast line (*Stutz and Pilkey*, 2001). These islands are sometimes part of a barrier island system, consisting of multiple barrier islands in line. In between these barrier islands, tidal inlets exist. According to *Davis Jr. and Fitzgerald* (2020), tidal inlets are openings in the coast line, through which the back-barrier basin is in contact with a sea or ocean and where the currents are primarily driven by tides. Tidal inlets are often closed embayments. When part of a barrier island system, two tidal inlets are connected through the back-barrier basin.

A prime example of such a barrier island system is located along the northern Dutch coast, the German coast and the western coast of Denmark, named the Wadden Sea (Fig. 1). Others are found along the east coast of the United States of America (*Davis Jr. and Fitzgerald*, 2020).

The Wadden Sea is considered as one of the most beautiful parts of the Netherlands and is an UNESCO World Heritage Site, proving the uniqueness of this region. The Dutch part of this barrier island system consists of seven major islands (Texel, Vlieland, Terschelling, Ameland, Schiermonnikoog, Rottumerplaat and Rottumeroog) and six tidal inlets (Marsdiep/Texel Inlet, Eierlandse Gat Inlet, Vlie Inlet, Ameland Inlet, Frisian Inlet and Eems-Dollard Inlet) (Fig. 1). In the Wadden Sea, some major sand banks are present. Examples are Richel and Griend (both near Vlieland and Terschelling) and Engelsmanplaat (located inside the Frisian Inlet).

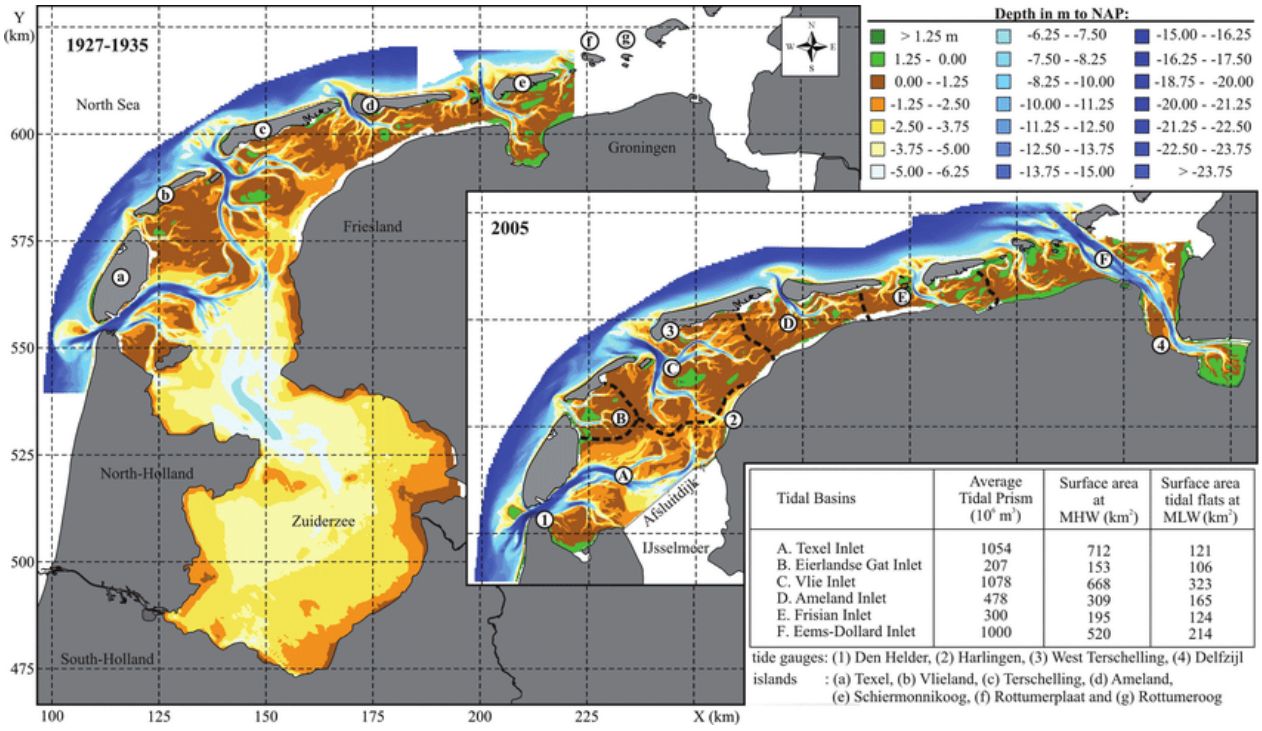

Tidal Basins	Average Tidal Prism (10^6 m^3)	Surface area at MHW (km^2)	Surface area tidal flats at MLW (km^2)
A. Texel Inlet	1054	712	121
B. Eierlandse Gat Inlet	207	153	106
C. Vlie Inlet	1078	668	323
D. Ameland Inlet	478	309	165
E. Frisian Inlet	300	195	124
F. Eems-Dollard Inlet	1000	520	214

tide gauges: (1) Den Helder, (2) Harlingen, (3) West Terschelling, (4) Delfzijl
islands : (a) Texel, (b) Vlieland, (c) Terschelling, (d) Ameland, (e) Schiermonnikoog, (f) Rottumerplaat and (g) Rottumeroog

Figure 1: Map of the Dutch part of the Wadden Sea showing the seven major islands and the six tidal inlets. The depth, measured from NAP (Normaal Amsterdams Peil), of the Wadden Sea for the period of 1927-1935 and for 2005 is also given. Obtained from *Elias et al.* (2012).

One of the major channels in this area, connects the Marsdiep Inlet (between Texel and Den Helder) with the Vlie Inlet (between Vlieland and Terschelling). The back-barrier basin consists of

a labyrinth of channels and tidal flats, where the latter is exposed during low tides and submerged during high tides. This region attracts around 1.3 million tourists a year (in 2015) (*CBS*, 2016), which stimulates its economy. The tidal flats and sandbanks allow special-made ships to run dry during low tide and continue their journey during high tide, which has become a sport many sailors enjoy (see the cover image).

The astronomical tide of the Wadden Sea, interpreted here as variations in the water level, changes over the basin. In the south, near Marsdiep, the tidal amplitude is the lowest (flood peak around 50 cm) and it increases when following the outer coast of the Wadden Sea northwards (flood peak around 75 cm near the Vlie Inlet), see Fig. 2. The tides are semi-diurnal, but the magnitude of the flood and ebb may differ within a day, so the first flood might be higher than the second flood. In Fig. 2, the astronomical tide at the Marsdiep Inlet and at the Vlie Inlet is presented.

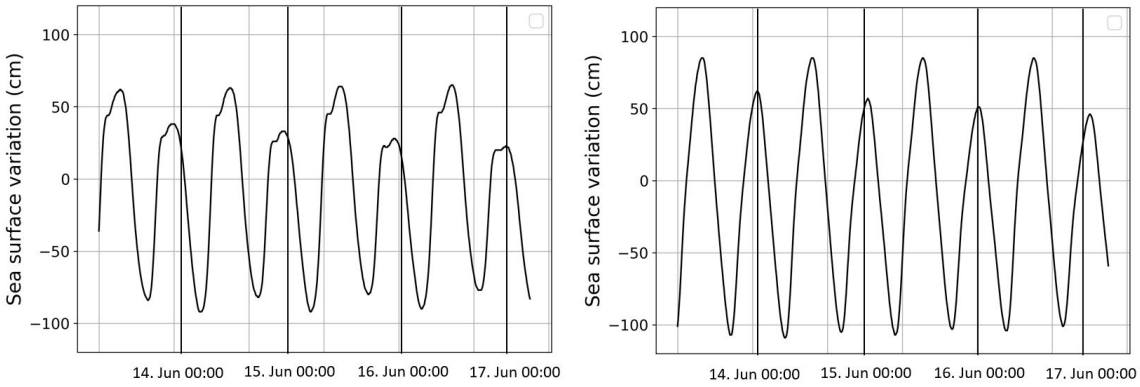

Figure 2: Calculated astronomical tide (sea surface variations) at the Marsdiep Inlet (left graph) and for the Vlie Inlet (right graph) for a period from 14 June 2021 till 18 June 2021. It is shown that the amplitude of the tidal wave increases and a small delay in flood/ebb occurs from the Marsdiep Inlet to the Vlie Inlet. Data obtained from https://www.rijkswaterstaat.nl/water/waterdata-en-waterberichtgeving/waterdata/getij.

The tidal currents consist of different tidal constituents: the principal lunar semi-diurnal M2-tide, a residual tide (M0), overtides (M4) with a frequency twice that of the M2-tide and other tidal constituents (*Gerkema*, 2019). The overtides are generated through non-linear self-interactions of the M2-tidal wave, by the means of friction, advection and excess mass flow in shallower waters (*Parker*, 1991; *Gerkema*, 2019). The perfect sinusoidal behaviour of the M2-tide becomes asymmetric caused by the generated M4-overtides in a shallower basin (*Van de Kreeke and Robaczewska*, 1993). The overtides and the residual currents are the determining factor in sediment transport. Since the M2-tide is a perfect sinusoidal function, the net inflow equals the net outflow. Due to the asymmetry introduced by the overtides and the residual current, the inflow and outflow do not cancel, resulting in a net sediment transport through the tidal inlet (*Van de Kreeke and Robaczewska*, 1993).

The sediment transport increases according to a higher order power (faster than linear) of the current (*Soulsby*, 1997). So a small change in current has a significant influence on the associated sediment transport. Due to this sediment transport, the morphology of the tidal inlet changes, which in turn affects the hydrodynamics of the system. This feedback mechanism is important to understand, since changes in morphology may cause tidal flats to disappear or the back-barrier basin to silt up.

The future of tidal inlet systems is uncertain, due to climate change and the accompanied accelerated sea level rise these diverse habitats may change. Sea level rise causes the basin to become deeper over time without the need of a net sediment export. In order for tidal flats to keep pace with the rising sea level, a net import must thus exist to counteract the deepening of the basin. Due to the sea level rise, the system remains out of equilibrium until a new equilibrium is found where the net import of sediments compensates for sea level rise (*Van Goor et al.*, 2003).

To gain insight in the hydrodynamics and morphodynamics of a tidal inlet system, one often has two options to rely on. First, numerical models are used to calculate water motion, sediment transport and morphological changes in such systems (e.g. (*Dissanayake et al.*, 2012; *Wang et al.*, 2018)). With numerical models, one can approach a differential equation and find approximate solutions for systems even when no analytical solutions exist. The main advantage is therefore that numerical modelling provides a quasi-realistic outcome. This comes with a cost: morphodynamic simulations take long (days to weeks) and are therefore not suitable for studies on the sensitivity of the model to certain parameters. Furthermore, it is hard to determine which driving mechanism is responsible for a certain process.

A second option relies on finding analytical solutions for a simplified system. Analytical solutions have disadvantages and advantages over numerical modelling. The main disadvantage of using analytical solutions derived from a simplified model is that they generally provide much less detail and are therefore less realistic. However, analytical solutions also provide some benefits. Firstly, analytical solutions consume much less time and computer power and therefore the evolution of the basin can be calculated much further into time. This also allows for studying the sensitivity of the model with respect to certain parameters. Furthermore, analytical solutions can be decomposed into different forcing mechanisms and thus provide more physical insight compared to numerical models.

Multiple studies have been conducted on this topic, where the hydrodynamics, sediment transport and/or morphological evolution of a simplified system are studied. Here, the models of some of those studies are briefly outlined. *Schuttelaars and de Swart* (1997) presented a model on the morphological evolution of a simplified basin. Here, a tidal embayment is simplified as a straight channel with a varying bottom. Furthermore, variations in width of the channel are neglected. *Schuttelaars and de Swart* (1997) only considered the evolution of the bed of the embayment and take both bed load and suspended sediment transport into account. This has been performed with and without the presence of an overtide. *Todeschini et al.* (2008) presented a model of a one-dimensional channel with an exponential decreasing width, when moving further into the basin, and a non-uniform bottom. For this channel, the morphological evolution is determined using a numerical approach on the one dimensional shallow water equations.

A third study using a simplified model, where analytical solutions are found, is conducted by *Frankemölle* (2020). In this research, a straight one-dimensional tidal embayment with one opening and homogeneous depth is considered with an incoming M2-tide. Furthermore, radiative damping was assumed to be absent and imported sediment was uniformly distributed over the length and depth of the embayment. *Frankemölle* (2020) considered both the tidally driven currents, the sediment transport and the morphological evolution (with focus on finding stable equilibria) under the influence of sea level rise.

All presented studies only focus on a single tidal inlet. A study on the stability of a double tidal inlet system was performed by *Van de Kreeke* (1990). Here, it was assumed that the sediment is eroded/deposited only in the tidal inlet (*Van de Kreeke*, 1985). No simplified model exists where the hydrodynamics and the morphological evolution under influence of sea level rise of an double tidal inlet system with radiative damping is considered, where erosion/deposition occurs in the back-barrier basin.

In this study, the hydrodynamical and morphological evolution of such a simplified double tidal-inlet system is studied using a similar method presented by *Frankemölle* (2020). The double tidal inlet system is approximated by a channel with two entrances. The main goal of this study is to gain insight into the morphological evolution of an arbitrary sized double tidal inlet system, with and without the influence of sea level rise. In order to compute the morphological evolution, insight on the hydrodynamics and sediment transport in the tidal basin is required. Here, attention will be paid specifically to the different hydrodynamical processes causing sand transport and how these processes change for different basin sizes. The theory will be applied to a realistic basin in order to gain insight into its morphological processes and evolution. Here, the Marsdiep-Vlie system is chosen as the case study (prototype), but the theory can be applied to any double inlet system under the influence of a tidal forcing.

The structure of this study will be as follows. In Section 2, the model and the governing equations for the water motion, sediment transport and evolution are presented. In Section 3, the governing equations are solved to obtain approximate analytical solutions for the model. Then the methods (Section 4) and the accompanied chosen parameter values are given. The results of this study are presented in Section 5. In Section 6, the discussion is given and Section 7 contains the conclusions.

2 Model and model analysis

In this section, the model is formulated and analyzed. First, the domain is sketched. Next, the governing equations and boundary conditions are stated. After that, the sediment transport will be discussed and linked to time evolution, which includes equations for the changes in depth and length of the basin. Finally, the model will be put in dimensionless form using appropriate scaling relations.

The model consists of three components (Fig. 3). The first is the hydrodynamics of the system. These hydrodynamical processes induce a sediment transport. Due to the sand transport, a net sediment flux into or out of the basin is present, resulting in a change in morphology. These changes are expressed in terms of changes in the depth and length of the basin. The hydrodynamics changes due to the changed basin size (meaning depth and length), in turn changing the sand transport and so forth. The structure of the model can be schematically depicted as in Fig. 3.

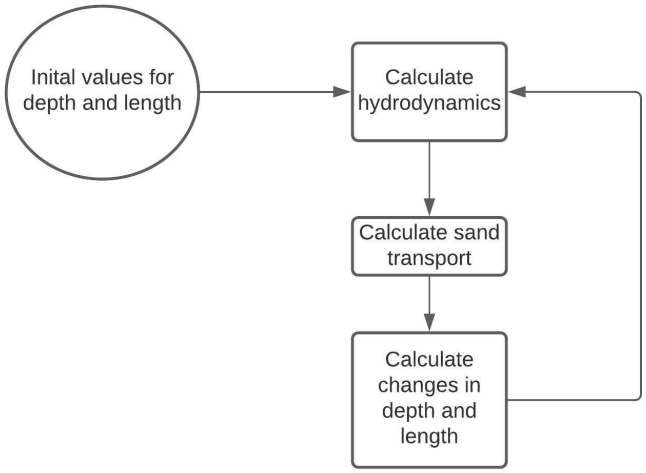

Figure 3: The structure behind the model is presented in this flow chart. For a certain initial depth and length of the basin the hydrodynamics and sand transport are calculated. From this, the changes in length and depth are obtained. Using the new basin size, the hydrodynamics are again calculated and so forth.

2.1 Domain and environmental setting

In order to compute the hydrodynamics and the morphological changes, an one-dimensional straight channel with two entrances is considered and radiative damping is taken into account by allowing waves to leave the system at both entrances. The channel has a constant depth H and a length L_b, extending from $x = -L$ to $x = L$ (where $L = L_b/2$), and a sea surface level η, measured from the undisturbed water level (Fig. 4). Due to the constant depth, the imported/exported sediment spreads out homogeneously over the channel.

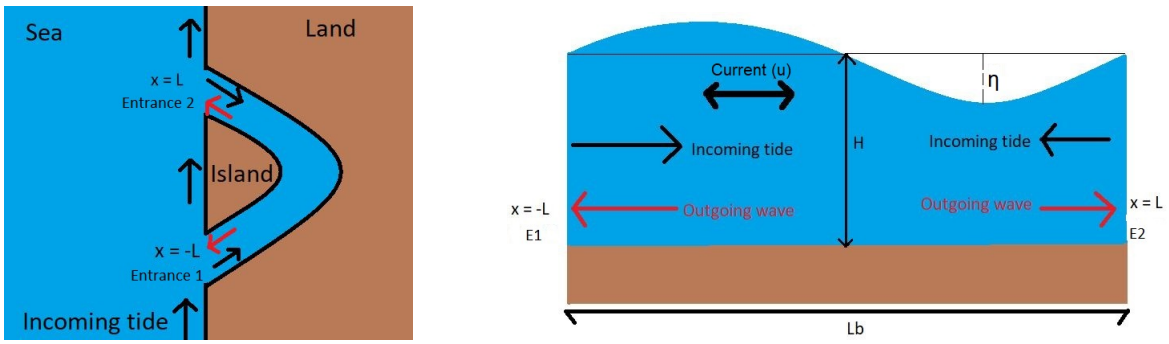

Figure 4: Left: Top view of the domain showing the open channel with the two entrances. The black arrows indicate the incoming tide and the red arrows indicate the outgoing wave (radiative damping). Right: Along-section of the system with a uniform depth H and a basin length L_b, where E1 and E2 represents the first and second entrance.

2.2 Governing hydrodynamical equations

Similar to *Frankemölle* (2020), the one-dimensional shallow water equations are used, which read

$$\frac{\partial u}{\partial t} + u\frac{\partial u}{\partial x} = -g\frac{\partial \eta}{\partial x} - \frac{C_d|u|u}{H+\eta}, \tag{2.1a}$$

$$\frac{\partial \eta}{\partial t} + \frac{\partial}{\partial x}[(H+\eta)u] = 0. \tag{2.1b}$$

Here, x is the x-coordinate, t is time and u is the cross-sectionally averaged velocity in the x-direction, η is the level of the sea surface with respect to the undisturbed sea, H is the undisturbed water depth and C_d is the friction coefficient. On both entrances, an incoming tidal wave with angular frequency ω is imposed. At the first entrance (at $x = -L$), the incoming tidal wave has an amplitude Z. For the second entrance (at $x = L$), the amplitude becomes αZ, where α is a scaling factor. Both incoming tidal waves follow a sinusoidal behaviour, allowing a phase shift ϕ to be present. Furthermore, radiative damping is taken into account. In principle, the damping wave leaving at entrance 2, will travel along the coastline and re-enter at entrance 1 (same for waves leaving entrance 1). In this study it is assumed that the distance over sea between inlets is large, then the damping wave will be fully damped before re-entering and therefore will not be taken into account. In total, at each entrance there will be an incoming tidal wave and a leaving damping wave (Fig. 4). The considerations above result in the following boundary conditions:

$$\eta_1^{in} = Z\cos(\omega t) : \text{ at } x = -L, \tag{2.2a}$$

$$\eta_2^{in} = \alpha Z\cos(\omega t - \phi) : \text{ at } x = L. \tag{2.2b}$$

Note that the boundary conditions concern the incoming tidal wave. This allows for outwards travelling waves (radiative damping), which are determined by the system itself. The depth H and length L_b depend on time and are therefore variables of state. For this reason, the model is not closed and additional equations are needed to describe the changes in undisturbed depth and length of the basin. This will be presented in Section 2.3.

2.3 Sediment transport rate and time evolution

Soulsby (1997) states that the suspended transport rate and the bed load transport rate follow the same behaviour (in terms as a power of the current), but with different pre-factors, for sediment transport driven by waves and currents (Soulsby-van Rijn equation). In this study the total load (sediment transport rate) is taken proportional to the velocity cubed (*Bagnold*, 1973; *The Open University*, 1999), such that;

$$q = \hat{q}u^3. \tag{2.3}$$

Here $\hat{q}$ is a proportionally factor dependant on the system and q is the sediment transport rate in m^2/s. The reasoning of *Bagnold* (1973) and *The Open University* (1999) behind Eq. (2.3) is that the sediment transport rate is proportional to the power of the current, which in turn is proportional to the current cubed.

The time evolution of the morphology is based on four assumptions. First, the imported sediment spreads out homogeneously over the basin. The same applies to the export, where the sediment is eroded and transported away and after leaving the basin spreads out homogeneously. A certain amount of the deposited/eroded sediment contributes to the depth, while the rest contributes to the length of the basin (*Frankemölle*, 2020). Furthermore, it is assumed that the values for α and ϕ do not change when the basin length changes and therefore stays constant over time. In a physical sense this is interpreted that the two entrances remain on the same position, but the channel gets smaller/larger in the back-barrier region, due to deposition/erosion. Thirdly, within a given time, the basin does not change significantly and therefore the basin size and the sediment transport rate are constant within that given time (*Frankemölle*, 2020). Lastly, the net sediment transport between the two entrances is the determining factor for import/export of sediment, based on a similar argument made for a single inlet by *Frankemölle* (2020). Since there are two entrances, the latter assumption is written as:

$$q_{net} = q_1 - q_2 + q_{wave}. \tag{2.4}$$

Here, q_{net} is the net sediment transport of the entire channel and q_1 and q_2 are the sediment transport at entrance 1 and 2 respectively. Furthermore, q_{wave} is the sediment import by waves due to littoral drift along the coast. Since import for entrance 1 runs in the positive direction and the import of entrance 2 runs in negative direction (vice versa for export), a minus sign is added to the transport at the second entrance to ensure that import is always positive and export is always negative.

To obtain expressions for the changes in depth and length of the basin, the method described by *Frankemölle* (2020) is used. First the mass balance of the system is specified:

$$(1-p)d(HL_b) = -q_{net}dt, \tag{2.5}$$

in which dt is some increment of time, p is the porosity and q_{net} is the net sediment transport. Some part of the sediment import or export concerns changes in depth $(1-a)$ and the other part for the length of the basin (a), where a is the fraction coefficient. Using this, Eq. (2.5) becomes

$$\begin{aligned} \frac{dL_b}{dt} &= \frac{-aq_{net}}{(1-p)H}, \\ \frac{dH}{dt} &= \frac{-(1-a)q_{net}}{(1-p)L_b}. \end{aligned} \tag{2.6}$$

Since the morphological evolution under influence of sea level rise SLR is also studied, Eq. (2.6) changes to:

$$\begin{aligned} \frac{dL_b}{dt} &= \frac{-aq_{net}}{(1-p)H}, \\ \frac{dH}{dt} &= \frac{-(1-a)q_{net}}{(1-p)L_b} + SLR. \end{aligned} \tag{2.7}$$

2.4 Non-dimensionlizing the model

In the previous of this section, the model is presented. Now, in order to construct approximate solutions, their dimensionless form needs to be introduced. To do so, for each variable an appropriate scaling factor is chosen. In line with *Frankemölle* (2020), the time is scaled with the inverse of the tidal angular frequency, thus $t = \omega^{-1}\tilde{t}$. Here, the tilde indicates that the variable is dimensionless. Furthermore, the distance x is scaled as $x = (\sqrt{gH}/\omega)\tilde{x}$, where $L_t = \sqrt{gH}/\omega$ is the frictionless tidal wavelength (including an extra factor of $(2\pi)^{-1}$ in the denominator due to in the angular frequency), meaning that $\tilde{x}$ changes when H changes. The basin length is written as $L_b = L_t\tilde{L}_b$. Next, the wave height η is be scaled by amplitude Z, such that $\eta = Z\tilde{\eta}$. Lastly, in Eq. (2.1a) both linear and non-linear terms are present. It is known that in most tidal inlet system, the tidal dynamics is linear to a first order approximation, therefore the linear terms should be of the same order of magnitude and the same holds for the non-linear terms. Therefore, one can write that $\frac{\partial u}{\partial t} \sim g\frac{\partial \eta}{\partial x}$ from which follows that the current scales with U $= \sqrt{\frac{g}{H}}Z\tilde{u}$. The dimensionless form of the shallow water equations are then obtained by plugging in the scaling factor in Eqs. (2.1a) and (2.1b), namely (after dropping the tildes):

$$\frac{\partial u}{\partial t} + \epsilon u\frac{\partial u}{\partial x} = -\frac{\partial \eta}{\partial x} - \frac{\gamma|u|u}{1+\epsilon\eta}, \tag{2.8a}$$

$$\frac{\partial \eta}{\partial t} + \frac{\partial}{\partial x}[(1+\epsilon\eta)u] = 0. \tag{2.8b}$$

Furthermore, the dimensionless boundary conditions are rewritten as

$$\eta_1^{in} = \cos(t);\ \text{at } x = \text{-}\ell, \tag{2.9a}$$

$$\eta_2^{in} = \alpha\cos(t-\phi);\ \text{at } x = \ell. \tag{2.9b}$$

In this dimensionless form, three extra parameters are defined:

$$\gamma = \omega^{-1}ZC_d\frac{g^{1/2}}{H^{3/2}}, \quad \ell = \frac{L_b}{2L_t} \quad \text{and} \quad \epsilon = \frac{Z}{H}. \tag{2.10}$$

Note that $\ell = \tilde{L}_b/2$. Here, ϵ scales the magnitude of the non-linear terms compared to the linear terms. Since the water depth is in general greater than the sea level deviation, ϵ is generally much smaller than 1.

A final modification to the shallow water equations must be performed, i.e., the quadratic friction term needs to be linearized. Following *Lorentz* (1926), the assumption is made that the amount of tidal energy lost over one tidal cycle in the entire basin must be equal for both the quadratic and

the linear friction term. This way, the dimensionless momentum equation (Eqs. (2.8a)) is rewritten as (*Frankemölle*, 2020)

$$\frac{\partial u}{\partial t} + \epsilon u \frac{\partial u}{\partial x} = -\frac{\partial \eta}{\partial x} - \frac{\lambda u}{1+\epsilon\eta}. \tag{2.11}$$

Here, λ is the linearized friction coefficient and it is given by

$$\lambda = \gamma \frac{\int_{-\ell}^{\ell} \langle |u^3| \rangle \, dx}{\int_{-\ell}^{\ell} \langle |u^2| \rangle \, dx}. \tag{2.12}$$

Note here that λ is proportional to the current u and therefore a higher current means an increase in bottom friction. From calculations it follows that for most basins sizes it holds that $\lambda \sim 1$. Only for deep basins, the linearized friction coefficient becomes very small.

Next, the sediment transport and time evolution are put in dimensionless form. The sediment transport rate (Eq. (2.3)) scales with $\hat{q}U^3$, therefore the dimensionless form of Eq. (2.4) becomes:

$$\tilde{q}_{net} = \tilde{q}_1 - \tilde{q}_2 + \tilde{q}_{wave}. \tag{2.13}$$

Since the net sediment transport rate (Eq. (2.13)) is dimensionless, Eq. (2.7) is also rewritten into dimensionless form using Eq. (2.10), $H = H_0\tilde{H}$, where H_0 is a reference depth, and the fact that sea level rise scales with H_0/ω^{-1}. The changes in dimensionless depth and length are given by (after dropping the tildes)

$$\begin{aligned} \frac{dL_b}{d\tau} &= \frac{-aq_{net}}{H^3}, \\ \frac{dH}{d\tau} &= \frac{-(1-a)q_{net}}{\ell H^2} + SLR. \end{aligned} \tag{2.14}$$

Note that SLR is now the dimensionless sea level rise. The morphological time-coordinate (τ) is defined as

$$\tau = \frac{t}{T_{morf}}, \tag{2.15}$$

where T_{morf} (morphological time scale) is given by

$$T_{morf} = \frac{H_0^3(1-p)}{\hat{q}gZ^3}. \tag{2.16}$$

To solve Eq. (2.14), initial values for the undisturbed depth ($H(t=0)$) and basin length ($L_b(t=0)$) are needed, which will be elaborated on in Section 4.

3 Solving the model

First, perturbation theory is used to obtain the differential equations for the tidal hydrodynamics for the zeroth and first order. Secondly, analytical solution of these differential are obtained. Using the equations on zeroth and first tidal current and sea surface variation, equations of the tidally averaged sediment transport and the associated time evolution of the basin are obtained.

3.1 Tidal hydrodynamics of the dominant (zeroth) and first order

Eqs. (2.8b) and (2.11) for the water motion are not solvable exactly due to non-linearity and the time-dependence of H and L_b. Therefore, an approximate solution has to be constructed. This is only possible when the non-linear terms are small compared to the linear terms. This is assumed to be true for the tidal dynamics in a shallow tidal basin. Since ϵ is taken to be much smaller than 1 (see previous section), it is a valid parameter to use for the scaling in the perturbation series. The other parameters of the model (ℓ and λ) are both of order 1 and therefore not suitable for perturbation theory. The series are defined as follows for the current u and sea level deviation η:

$$u(x,t) = u_0(x,t) + \epsilon u_1(x,t) + h.o.t. \tag{3.1}$$

$$\eta(x,t) = \eta_0(x,t) + \epsilon \eta_1(x,t) + h.o.t. \tag{3.2}$$

where $h.o.t.$ stands for higher order terms (above first order) in terms of ϵ. All higher order terms above the first order term are assumed to be small enough compared to the first two terms such that they can be neglected. The friction term of Eq. (2.8b) is approximated using a Taylor expansion and upon inserting the perturbed current and sea level deviation (Eqs. (3.1) and (3.2)) into Eqs. (2.8a) and (2.8b), the following system of equations are obtained by sorting in leading order terms and terms in ϵ (first order). The zeroth order system becomes

$$\frac{\partial u_0}{\partial t} + \frac{\partial \eta_0}{\partial x} + \lambda u_0 = 0, \tag{3.3a}$$

$$\frac{\partial \eta_0}{\partial t} + \frac{\partial u_0}{\partial x} = 0. \tag{3.3b}$$

The dimensionless boundary conditions (Eqs. (2.9a) and (2.9b)) also need to be rewritten in leading order. Since the tidal sea surface height at both inlets is assumed to be composed of only an incoming/external tide of frequency ω, the dimensionless boundary conditions of the zeroth order are equal to Eqs. (2.9a) and (2.9b), but then the left hand side of the equations reads η_0^{in} instead of η^{in}.

The first order solution follows from a collection of all the terms that are of order ϵ. The continuity and momentum equation for the first order system reads

$$\frac{\partial u_1}{\partial t} + \underbrace{u_0 \frac{\partial u_0}{\partial x}}_{\text{Advective}} = -\frac{\partial \eta_1}{\partial x} + \underbrace{\lambda u_0 \eta_0}_{\text{Friction}} - \lambda u_1, \tag{3.4a}$$

$$\frac{\partial u_1}{\partial x} + \underbrace{\frac{\partial}{\partial x}[u_0 \eta_0]}_{\text{Excess mass flux}} + \frac{\partial \eta_1}{\partial t} = 0. \tag{3.4b}$$

The advection term represents the advected tidal momentum by the tidal current and the friction term the current generated through the depth-dependent friction. The excess mass flux concerns a flow compensating for the import of mass by waves. In Eqs. (3.4a) and (3.4b) the three non-linear forcing terms are given, namely the friction, excess mass flux and advection. The first order dimensionless boundary conditions at the two inlets become

$$\eta_1^{in} = 0; \text{ at } x = \text{-}\ell, \tag{3.5a}$$

$$\eta_1^{in} = 0; \text{ at } x = \ell. \tag{3.5b}$$

In the next section, solutions of the zeroth-order and first-order systems will be obtained.

3.2 Solution of the zeroth-order system

Since the boundary conditions are stated in terms of η_0, it is convenient to obtain a differential equation in terms of η_0. To do so, the x-derivative of the momentum equation (Eq. (3.3a)) and the time derivative of the continuity equation (Eq. (3.3b)) are taken. This way, the zeroth order current (u_0) is eliminated from this system of equations and a single partial differential equation in term of η_0 is obtained, given by

$$\frac{\partial^2 \eta_0}{\partial t^2} + \lambda \frac{\partial \eta_0}{\partial t} - \frac{\partial^2 \eta_0}{\partial x^2} = 0. \tag{3.6}$$

To solve this equation, it is used that tides are nearly sinusoidal and that the boundary conditions are stated in terms of cosines. Here, only interest is paid to the non-transient solutions, since the transient solution part relates to the initial conditions. This invites for a separation of variables using a complex exponential for the time dependence:

$$\eta_0(x,t) = \Re\left[\hat{\eta}_0(x) e^{-it}\right], \tag{3.7}$$

where $\Re$ stands for the real part of a complex function or number. By plugging this ansatz into Eq. (3.6) after rewriting and eliminating the complex exponential after differentiation, the following equation is obtained:

$$\frac{d^2 \hat{\eta}_0(x)}{dx^2} + \kappa_0^2 \hat{\eta}_0(x) = 0, \tag{3.8}$$

where κ_0 is given by

$$\kappa_0 = \sqrt{1 + i\lambda}. \tag{3.9}$$

The boundary conditions also change, since $\cos(t) = \Re[e^{-it}]$ and $\cos(t - \phi) = \Re[e^{-i(t-\phi)}]$. The boundary conditions (Eqs. (2.9a) and (2.9b)) are written in terms of $\hat{\eta}_0$:

$$\hat{\eta}_0^{in}(x) = 1 \text{ at } x = \text{-}\ell. \tag{3.10a}$$

$$\hat{\eta}_0^{in}(x) = \alpha e^{i\phi} \text{ at } x = \ell. \tag{3.10b}$$

Note that, Eq. (3.8) is an ordinary differential equation with the general solution

$$\hat{\eta}_0(x) = A e^{i\kappa_0 x} + B e^{-i\kappa_0 x}. \tag{3.11}$$

Here, A and B are integration constants to be determined using the boundary conditions (Eqs. (3.10a) and (3.10b)). Since the time dependence is given by $\hat{\eta}_0(x)$ multiplied by e^{-it}, the first term of Eq. (3.11) represents a wave travelling in the positive direction and the second term is a wave travelling in the negative direction. Due to the presence of radiative damping, at $x = \ell$ the incoming tidal wave (given by Eq. (3.10a)) is known, but the damping wave is not known. Therefore, this boundary condition can only be applied on the positive travelling wave (first term) of Eq. (3.11), since the negative travelling wave at the same location is unknown and to be determined by the system itself. The same applies at $x = \ell$ for the other boundary condition (Eq. (3.10b)) and the negative travelling wave. The constants of integration then become

$$A = e^{i\kappa_0 \ell}, \tag{3.12}$$

$$B = \alpha e^{i(\kappa_0 \ell + \phi)}. \tag{3.13}$$

Thus, the full solution for the zeroth order of the wave height reads

$$\hat{\eta}_0(x) = e^{i\kappa_0(x+\ell)} + \alpha e^{-i(\kappa_0(x-\ell)-\phi)}. \tag{3.14}$$

From the zeroth order (dimensionless) continuity equation (Eq. (3.3b)), it follows that;

$$\frac{\partial \eta_0}{\partial t} = -\frac{\partial u_0}{\partial x}. \tag{3.15}$$

Insert Eq. (3.11) into Eq. (3.15) to obtain an expression for $\hat{u}_0$;

$$\frac{d\hat{u}_0}{dx} = ie^{i\kappa_0(x+\ell)} + i\alpha e^{-i(\kappa_0(x-\ell)-\phi)}. \tag{3.16}$$

The integral of x is taken and the integration constant from this integration is set to zero. This is done, because for the zeroth order tide, the flood current should be equal but opposite to the ebb current. When a non-zero integration constant is introduced a translation occurs, causing this not to be the case. Using this, $\hat{u}_0$ becomes:

$$\hat{u}_0(x) = \frac{1}{\kappa_0} e^{i\kappa_0(x+\ell)} - \frac{\alpha}{\kappa_0} e^{-i(\kappa_0(x-\ell)-\phi)}. \tag{3.17}$$

3.3 Solution of the first-order system

Solutions of the first-order system are driven by those of the zeroth-order system and the latter are sinusoidal, with scaled frequency 1 (first two equations of Eq. (3.18)). When those expressions are substituted in Eqs. (3.4a) and (3.4b), it follows that the non-transient solutions of the first-order system consist of a time-independent (residual) component and an overtide that is sinusoidal with double the frequency of the zeroth-order tide (last two equations of Eq. (3.18)).

$$\begin{aligned}
u_0(x,t) &= \frac{1}{2}\hat{u}_0 e^{-it} + \frac{1}{2}\hat{u}_0^* e^{it}, \\
\eta_0(x,t) &= \frac{1}{2}\hat{\eta}_0 e^{-it} + \frac{1}{2}\hat{\eta}_0^* e^{it}, \\
u_1(x,t) &= \bar{u} + \frac{1}{2}\hat{u}_1 e^{-2it} + \frac{1}{2}\hat{u}_1^* e^{2it}, \\
\eta_1(x,t) &= \bar{\eta} + \frac{1}{2}\hat{\eta}_1 e^{-2it} + \frac{1}{2}\hat{\eta}_1^* e^{2it}.
\end{aligned} \tag{3.18}$$

Here, $\bar{u}$ and $\hat{u}_1$ are the currents and $\bar{\eta}$ and $\hat{\eta}_1$ are the tidal wave heights for the residual and first overtide tidal constituents respectively. Note that the asterisk gives the complex conjugate of the complex function.

These expressions are plugged into Eqs. (3.4a) and (3.4b) and are subsequently split into the two tidal constituents (residual and first overtide). For the residual tide, the system of equations is given by

$$\frac{d}{dx}\left[\bar{u} + \frac{1}{4}\hat{u}_0\hat{\eta}_0^* + \frac{1}{4}\hat{u}_0^*\hat{\eta}_0\right] = 0, \tag{3.19a}$$

$$\frac{1}{4}\left[\hat{u}_0\frac{d}{dx}\hat{u}_0^* + \hat{u}_0^*\frac{d}{dx}\hat{u}_0\right] = -\frac{d\bar{\eta}}{dx} + \frac{\lambda}{4}\left[\hat{u}_0\hat{\eta}_0^* + \hat{u}_0^*\hat{\eta}_0\right] - \lambda\bar{u}, \tag{3.19b}$$

with the boundary conditions

$$\bar{\eta}^{in}(x = -\ell) = 0 \quad \text{and} \quad \bar{\eta}^{in}(x = \ell) = 0. \tag{3.20}$$

When integrating Eq. (3.19a), the following equation is obtained:

$$\bar{u} + \underbrace{\frac{1}{4}\hat{u}_0\hat{\eta}_0^* + \frac{1}{4}\hat{u}_0^*\hat{\eta}_0}_{\text{Stokes velocity}} = \underbrace{\bar{u}_{1m}}_{\text{Through flow}}. \tag{3.21}$$

Here, the Stokes velocity is the mean velocity of a fluid parcel in the direction of the wave propagation, when transported by the orbital motion of a wave. The through flow (also known as the residual mass transport velocity) is generated by a pressure difference between the two entrances, where the pressure gradient results from a gradient in tidal sea surface variation between entrance 1 and 2. The solution to the through flow is determined in Appendix A.

The momentum and continuity equation for the first overtide become

$$-i\hat{u}_1 + \frac{1}{4}\hat{u}_0\frac{d}{dx}\hat{u}_0 = -\frac{1}{2}\frac{d}{dx}\hat{\eta}_1 + \frac{\lambda}{4}\hat{u}_0\hat{\eta}_0 - \frac{\lambda}{2}\hat{u}_1, \tag{3.22a}$$

$$\frac{d\hat{u}_1}{dx} = -\frac{1}{2}\frac{d}{dx}[\hat{u}_0\hat{\eta}_0] + 2i\hat{\eta}_1. \tag{3.22b}$$

Since the boundary conditions are stated in terms of the wave height, it is convenient to eliminate $\hat{u}_1$ from the system of equations (Eqs. (3.22a) and (3.22b)) and thus obtain a single equation in $\hat{\eta}_1$, as given in Appendix A (Eq. A.3). Solutions for $\bar{u}$, $\bar{\eta}$, $\hat{u}_1$ and $\hat{\eta}_1$ are derived in Appendix A. Note that Eq. (A.3) is linear, so the solution is the sum of responses to each of the three forcing terms in the right-hand side.

Since the expressions for the currents of the different tidal constituents are complex valued, their moduli and arguments are calculated. The modulus is of importance for the maximum allowed current for different basin settings and the argument is a key component in sediment transport, on which will be elaborated in the next section. The residual current is rewritten as:

$$\bar{u} = |\bar{u}|\cos(\phi_{res}). \tag{3.23}$$

Here, ϕ_{res} is the argument and $|\bar{u}|$ is the modulus of the residual current. For the other two tidal constituents, the expression of the current in terms of the modulus and the argument becomes

$$u_m = |\hat{u}_m| \cos((m+1)t - \phi_m). \tag{3.24}$$

Here, m gives the order of the solution. Note that u_1 applies for both the friction, advective and excess mass flux overtide and distinction will be made using superscripts.

3.4 Expressions for sediment transport

As mentioned earlier, the sediment transport is the driving force behind the evolution of the basin. When a net import occurs, the basin gets shorter and shallower. Whereas, when a net export occurs the basin becomes longer and deeper. For the evolution of a basin, the averaged sediment transport rate over one tidal cycle is of interest. Taking the average of the sediment transport over one tidal cycle is allowed, because the morphological timescale (Eq. (2.16)) is much larger than the tidal period. Therefore, the dimensionless sediment transport rate at every instant of time is averaged over one dimensionless tidal cycle:

$$\langle \tilde{q} \rangle = \frac{1}{2\pi} \int_0^{2\pi} \tilde{u}^3 dt. \tag{3.25}$$

Eq. (3.25) states that the total current is needed for the tidally averaged sediment transport. Remember that the first overtide consists of three components, generated by friction, excess mass flux and advection, hereafter abbreviated as Fr, EMF and ADV respectively. Using this knowledge, together with Eqs. (3.1), (3.23) and (3.24), the total current is written as

$$\begin{aligned} u = &|\hat{u}_0| \cos(t - \phi_0) + \epsilon \left(|\bar{u}| \cos(\phi_{res}) + \left|\hat{u}_1^{ADV}\right| \cos\left(2t - \phi_1^{ADV}\right) \right. \\ &\left. + \left|\hat{u}_1^{Fr}\right| \cos\left(2t - \phi_1^{Fr}\right) + \left|\hat{u}_1^{EMF}\right| \cos\left(2t - \phi_1^{EMF}\right). \right. \end{aligned} \tag{3.26}$$

Eq. (3.25) is integrated and worked out and sediment transport rate terms of order ϵ and ϵ^3 are found (*Ridderinkhof et al.*, 2014; *Frankemölle*, 2020). Since ϵ is small, the terms of order ϵ are much larger then the terms of order ϵ^3. Therefore, the order ϵ terms are dominant for the sediment transport rate. The total expression for the tidally averaged sediment transport rate is therefore written as

$$\langle q \rangle = \frac{3\epsilon |\hat{u}_0|^2}{2} |\bar{u}| \cos(\phi_{res}) + \frac{3\epsilon |\hat{u}_0|^2}{4} \left(\left|\hat{u}_1^{ADV}\right| \cos\left(\phi_1^{ADV} - 2\phi_0\right) + \right. \tag{3.27}$$

$$\left. \left|\hat{u}_1^{Fr}\right| \cos\left(\phi_1^{Fr} - 2\phi_0\right) + \left|\hat{u}_1^{EMF}\right| \cos\left(\phi_1^{EMF} - 2\phi_0\right) + h.o.t. \right. \tag{3.28}$$

Note that the for the first overtides, the phase difference between these overtides and zeroth-order solution is clearly of importance. Here, the $\cos(\phi_1 - 2\phi_0)$ determines not only the sign of the transport (and thus whether import or export occurs), but it is also a leading factor in determining the magnitude of the sediment transport caused by the overtides.

Using the dimensionless tidally averaged sediment transport rates, the expressions of the evolution of the depth and length of the basin are rewritten (Eqs. (3.29)). Furthermore, it is assumed that the changes in morphology of the basin occur slowly (Section 2) (*Frankemölle*, 2020). Therefore, Eqs. (3.29) can be discretized into an appropriate time step in which the tidally averaged sediment transport rate can be assumed constant, changing Eqs. (2.7) into:

$$\begin{aligned} \frac{\Delta L_b}{\Delta \tau} &= \frac{-a\langle q_{net}\rangle}{(1-p)H}, \\ \frac{\Delta H}{\Delta \tau} &= \frac{-(1-a)\langle q_{net}\rangle}{(1-p)L_b} + SLR. \end{aligned} \tag{3.29}$$

The discretization of Eqs. (3.29) follows a Forward Euler approach, where from initial conditions (initial basin depth and length), the time evolution of the morphology is determined. This way, the "old" basin size is used, to calculate the basin depth and length one step further in time. For this reason, the model is not fully analytical, but can be considered semi-analytical.

4 Model settings

In this study, a symmetrical and an asymmetrical case is considered. The difference between these two cases is the value for the parameters α and ϕ. Furthermore, an incoming M2 tide is imposed on the system. First, all default parameter values applicable to both case are presented in Table 1. These default parameters are the initial length L_{b0}, initial depth H_0 of the basin, tidal period T and frequency ω of the M2 tide, incoming M2 sea surface variation Z, friction coefficient C_d, fraction ratio a, the porosity p and the proportionality factor $\hat{q}$. Here, L_{b0}, H_0 and Z are based on the Marsdiep-Vlie channel. Therefore, the value of L_{b0} is fixed, while L_b can be any basin length (same for the depth). As a reminder, the basin length L_b and depth H depend on time and are therefore variables of state. The default basin length and depth (L_{b0} and H_0) are parameters of the system. Furthermore, the linearized friction coefficient λ depends on the basin size, α and ϕ and thus differ per system.

Table 1: Default parameter values based on the Marsdiep-Vlie channel, applicable to the symmetrical and the non-symmetrical case.

L_{b0}	70 km ($L_{b0}/L_t \sim 1$)
H_0	10 m (*Ridderinkhof et al.*, 2014; *Elias et al.*, 2012)
T	12 h and 25.2 min
ω	$1.405 \cdot 10^{-4}$ rad/s
Z	0.73 m (*Ridderinkhof et al.*, 2014)
C_d	$2.5 \cdot 10^{-3}$ (*Soulsby*, 1997)
a	0.5
p	0.4 (*Soulsby*, 1997)
$\hat{q}$	10^{-3} s^2/m

The last parameter value ($\hat{q}$) is based on a study performed by (*Wang et al.*, 2018), which states that the annual sedimentation in the western Wadden Sea is of the order millimeters per year. Now, the values of the parameters α and ϕ are discussed for both cases (and shown in Table 2). For the symmetrical case, it follows that $\alpha = 1$ and $\phi = 0$. However, for the non-symmetrical case, it is important to note that α and ϕ are parameters for the incoming tidal M2 wave. Values for these parameters need to be derived from measurements/data based on the total wave height (both incoming and outgoing wave). From the M2 amphidromic map of the North Sea (*Plüß*, 2003), the amplitude factor of the total wave (α_{tot}) is estimated to be 1.14 and the corresponding phase difference (ϕ_{tot}) is 0.52 rad.

Table 2: Default parameter values for the amplitude ratio and phase shift for the incoming wave for the symmetrical and the anti-symmetrical case.

	Symmetric	Non-symmetric
α	1	0.511
ϕ	0	0.604

In order to obtain α and ϕ from this, the model is used. For different values of α and ϕ, the corresponding α_{tot} and ϕ_{tot} are determined for the total wave in the model (Fig. 5). The values of α and ϕ for which holds that $\alpha_{tot} = 1.14$ and $\phi_{tot} = 0.52$ rad (black contour lines in Fig. 5) are chosen to be the appropriate parameter values to mimic the situation in the Marsdiep-Vlie channel. Using this method, the parameter values become: $\alpha = 0.511$ and $\phi = 0.604$ rad.

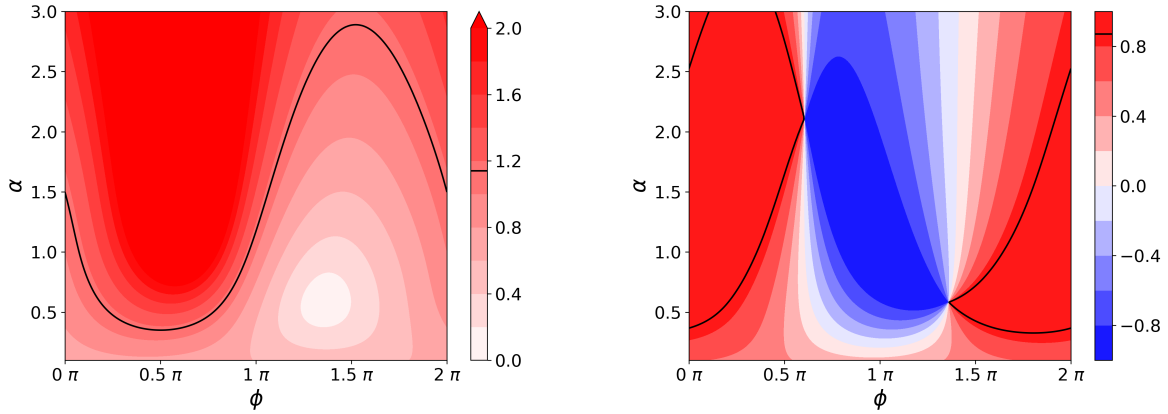

Figure 5: Colour plots of the amplitude ratio α_{tot} (left) and the cosine of the phase difference ϕ_{tot} (right) of the total M2 sea surface variation between entrances 1 and 2 as a function of the phase shift (between 0 and 2π) and amplitude ratio (between 0 and 3) of the incoming M2 wave between the two entrances. Here, the subscript "tot" refers to the total M2 sea surface variation (incoming and outgoing wave). The black lines indicate the contour lines for $\alpha_{tot} = 1.14$ (left) and $\cos(\phi_{tot})$ ≈ 0.87 (right).

The amplitude ratio α_{tot} and the total phase difference ϕ_{tot} between the two entrances for the total M2 tidal wave depends on the scaled basing length $L_b\mathrm{L}_t$ and the depth of the basin H for the non-symmetrical case. In Fig. 6, these two parameters are presented for different basin sizes, where the depth ranges from 3 to 50 m and is scaled by $H_0 = 10$ m and the scaled basin length ranges from 0.01 to 2π.

In this study, four experiments are performed on the time evolution of a basin with a certain initial length and depth. For each experiment, the time step Δt is equal to one year. In the first experiment, the time evolution of seven different initial basin sizes (initial depth and length) is studied in the absence of sea level rise and sediment import by waves. In the second experiment, the evolution is studied for the same basins, but now with a sea level rise corresponding to the current-day rate of 1.7 mm/yr (*Church et al.*, 2013). The third experiment also considers the current-day sea level rise, but also includes the net import of sediment by waves q_{wave} of 0.04. In the last experiment, a

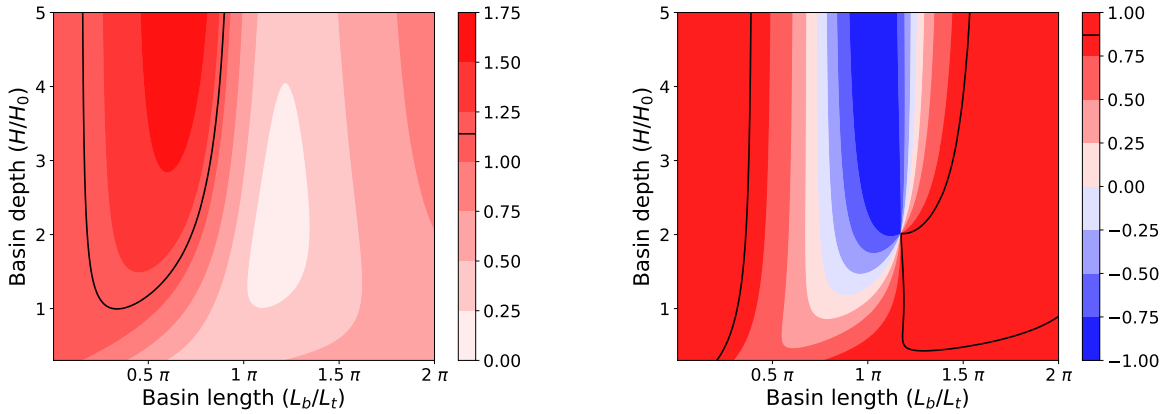

Figure 6: Colour plots of the amplitude ratio α_{tot} (left) and the cosine of the phase difference ϕ_{tot} (right) of the total M2 sea surface variation between entrances 1 and 2 as a function of the basin length scaled by $H_0 = 10$ m and the basin length scaled by the frictionless tidal wavelength. Here, the basin depth H is between 3 and 50 m . The scaled basin length L_b/L_t is between 0.01 and 2π, where L_t ranges from 38.6 km for 3 m depth and 157.6 km for 50 m depth. The subscript "tot" refers to the total M2 sea surface variation (incoming and outgoing wave). The black lines indicate the contour lines for $\alpha_{tot} = 1.14$ (left) and $\cos(\phi_{tot}) \approx 0.87$ (right).

sea level rise of 4.4 mm/yr (corresponding to the RCP2.6 scenario (*Church et al.*, 2013)) is added, combined with an import by waves of $q_{wave} = 0.04$. The latter corresponds to a dimensional import by waves around 470 m^2/yr for a basin of 10 m depth, which is a small fraction of the annual drift of 1-2 million m^3/yr estimated by *Van Veen* (1936). A higher value of q_{wave} is not chosen, because the import by waves would dominate over the tidal processes. In short, the four time evolution experiments are summarized below:

- Time evolution of seven different sized basin without sea level rise and sediment import by waves due littoral drift for 100,000 years.
- Time evolution of seven different sized basin with an annual sea level rise of 1.7 mm/yr and without sediment import by waves due to littoral drift for 4,000 years.
- Time evolution of seven different sized basin with an annual sea level rise of 1.7 mm/yr and a dimensionless import by waves of $q_{wave} = 0.04$, for 4,000 years.
- Time evolution of seven different sized basin with an annual sea level rise of 4.4 mm/yr and a dimensionless import by waves of $q_{wave} = 0.04$, for 4,000 years.

The difference in time between the first and the other experiments is due to the added sea level rise, which causes a large increase in depth when considered over long periods of time.

5 Results

In this section, the left column of a graph always represents the symmetric case and the right column the non-symmetric case. First, the values for the linearized friction coefficient λ are given for different basin lengths and depths for both cases. Second, the M2-tide is discussed, after which the M4- and M0-tides and the net import/export of sediment are shown. Lastly, the morphological evolution is presented.

5.1 Linearized friction coefficient

The dimensional linearized friction coefficient λ_{dim} is shown in Fig. 7 for the symmetric case (left) and the non-symmetric case mimicking the Marsdiep-Vlie channel (right). It reveals that the bottom friction decreases with increasing water depth and that for basins deeper than 10 m, the friction becomes very small. Furthermore, a maximum in bottom friction occurs around a basin length equal to half a tidal wavelength ($L_b/L_t = \pi$).

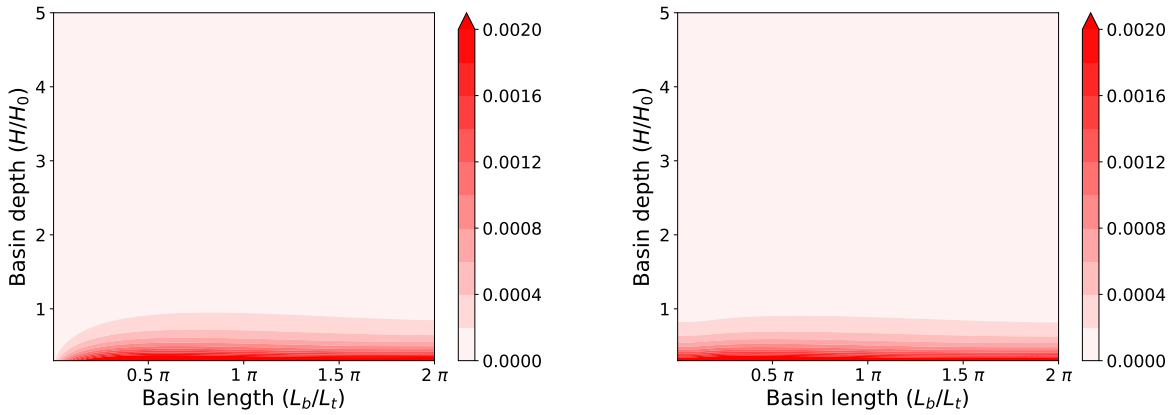

Figure 7: Colour plots of the dimensional linear friction coefficient λ_{dim} as a function of the scaled basin depth (H/H_0) and scaled basin length (L_b/L_t) for the symmetric system (left) and the asymmetric system that mimics the Marsdiep-Vlie channel (right). The parameter values of Table 1 are used. Here, the basin depth H is between 3 and 50 m and is scaled by $H_0 = 10$ m. The scaled basin length L_b/L_t is between 0.01 and 2π, where L_t ranges from 38.6 km for 3 m depth and 157.6 km for 50 m depth.

5.2 Dynamics of the M2-tide

In Fig. 8, times series of the dimensionless current of the left travelling, right travelling and the total wave of both cases for two tidal periods are shown. Here, the default parameter values of Table 1 are used. Since Fig. 8 represents the current for a single basin length and depth, the dimensionless and dimensional tidal wave only differ by a scaling factor and therefore show the same behaviour. The first row is for the entrance 1 and the second row at entrance 2. The left column gives the symmetrical case and the right column the non-symmetrical case. Furthermore, in Appendix B, the same graph (Fig. 21) is shown for the dimensionless sea surface variations.

The symmetric case (at both entrances) shows that the velocities at both entrances are equal in magnitude, but of opposite sign. Since $\alpha = 1$ and $\phi = 0$, the magnitude of the two incoming

flood/ebb currents are equal and both occur at the same instant of times. When flood occurs, the current at entrance 1 is positive, while the current at entrance 2 is negative (still flood due to wave travelling in opposite direction). Therefore, no current exists at the middle of the basin ($x = 0$). As a results, half of the system (from $x = -\ell$ to $x = 0$ or from $x = 0$ to $x = \ell$) has effectively become the system described by *Frankemölle* (2020), with the inclusion of radiative damping.

Furthermore, the effects of bottom friction is evident from the left panel of Fig. 8, showing the symmetric case. The right travelling wave at entrance 1 and the left travelling wave at entrance 2 have the same amplitude and initial phase. When the two waves at entrance 1 are considered it appears that the left travelling wave has undergone an amplitude and a local phase shift. The amplitude decreases is solely due to effects of bottom friction. The local phase shift is due to the effect of bottom friction and due to the fact that the left travelling wave has to cross the channel before it reaches entrance 1. Due to this distance, the flood of the left travelling wave lags the flood of the right travelling wave at entrance 1.

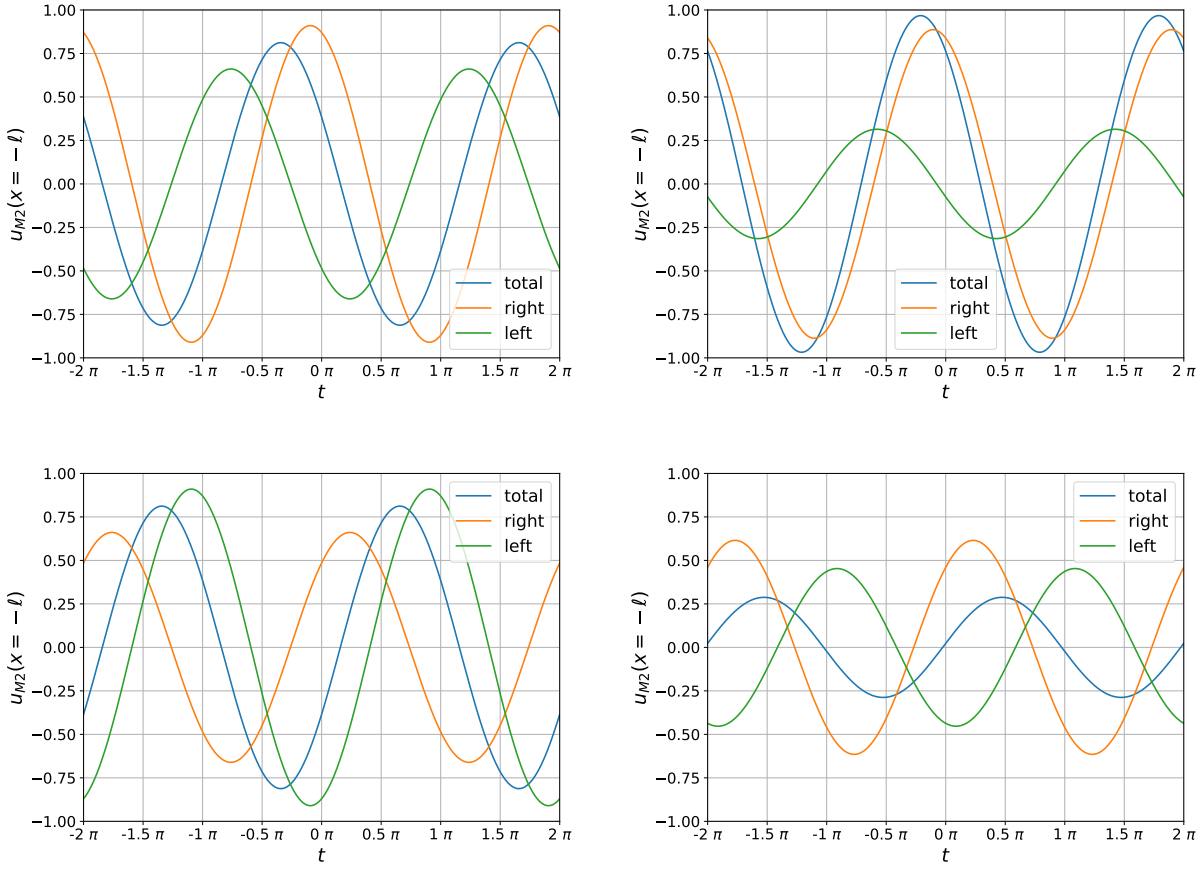

Figure 8: Time series of the dimensionless dominant tidal velocity induced by the left and right travelling wave and the total wave at the two entrances for two tidal periods. The first column is for the symmetric system and the second column for the non-symmetrical (mimicking the Marsdiep-Vlie channel) for a basin depth of 10 m and a basin length of 70 km. Furthermore, the first row indicates the first entrance and the second row gives the second entrance. The parameter values of Table 1 are used. The scaling parameter for the current is $U \approx 0.72$ m/s.

When the asymmetric case is considered, the same overall behaviour is observed. However, due to the introduction of the phase shift, more constructive interference occurs at entrance 1 and more destructive interference at entrance 2 for the current. For the sea surface variations (Appendix B, Fig. 21), the interference pattern is opposite. This results in a gradient between the two inlets, where the amplitude of the sea surface variation at entrance 1 is smaller compared to entrance 2. This in turns drives a negative current from entrance 2 to entrance 1, on which will be expanded when discussing the residual current. Furthermore, the peak current at entrance 2 is slightly lower than the peak current at entrance 1.

For the morphological evolution of the basin, the changes in amplitude of M2 currents at both entrances when depth H and length L_b change are important, because they are factors that determine the net import and export of sediment (Eq. (2.14)). In Fig. 9 the dimensional amplitude of the M2 tidal current is shown for different basin sizes. Furthermore, the phase of the M2 tidal current in itself is not important for the sediment transport, but the phase difference between the M2 and M4 tide is. The latter will be discussed in the next subsection.

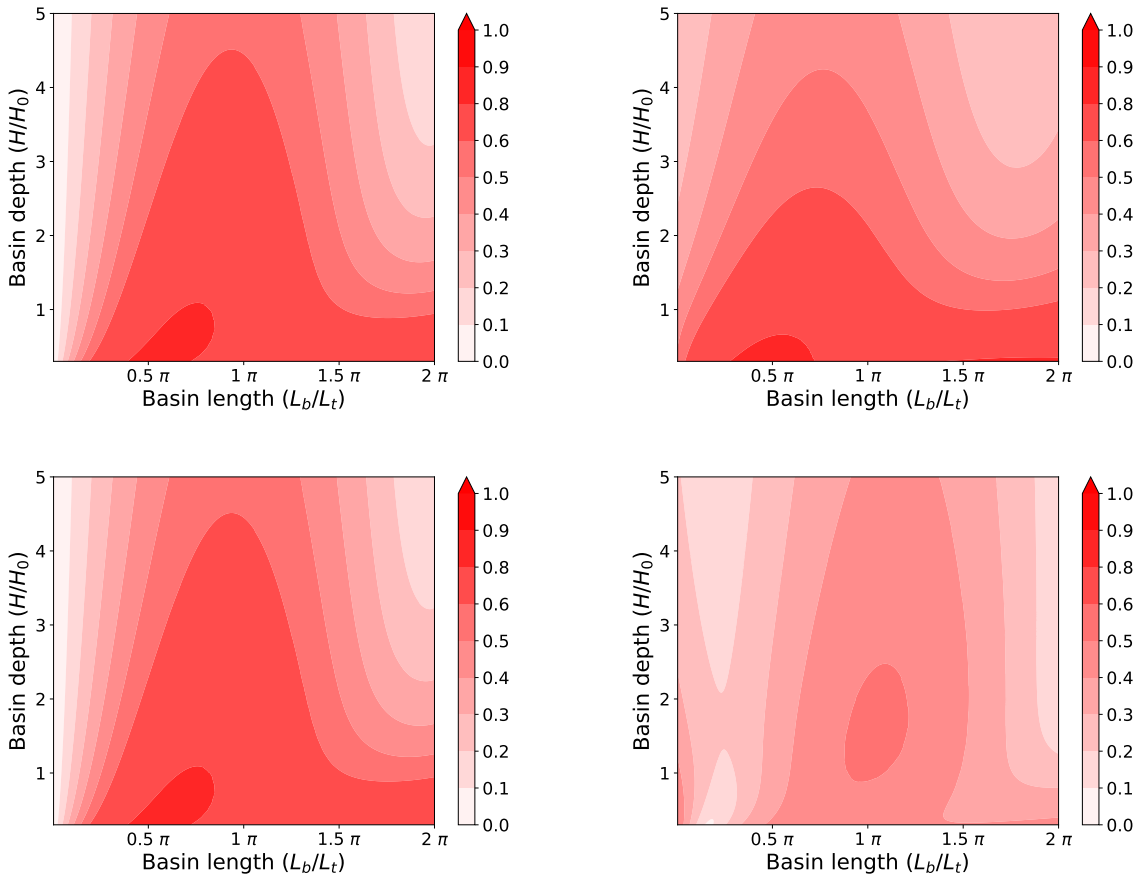

Figure 9: Colour plots of the dimensional amplitude of the M2 tidal velocity (m/s) as a function of scaled basin depth H/H_0 and scaled basin length L_b/L_t. Here, the basin depth H is between 3 and 50 m and is scaled by $H_0 = 10$ m. The scaled basin length L_b/L_t is between 0.01 and 2π, where L_t ranges from 38.6 km for 3 m depth and 157.6 km for 50 m depth. The first row represents the first entrance and the second row gives entrance 2. The parameter values of Table. 1 are used.

The left panel in Fig. 9 (symmetric case) shows that a resonance peak in the M2 tidal velocity occurs for a basin just shorter than half a tidal wavelength. When the basin length is half a tidal wavelength, the ebb at entrance 1 coincides with the flood at entrance 2 (so current in same direction), therefore amplifying each other. Due to friction, the resonance peak is slightly below half a frictionless tidal wavelength. The opposite occurs at a basin length close to the frictionless tidal wavelength, when ebb and flood flows balance each other out. Due to this interference, the amplitude of the M2 tidal velocity shows a "standing wave" behaviour with clear resonance peaks and troughs.

A slightly different behaviour is visible in the non-symmetrical case. Here, for entrance 1 a shift of the peak is shown to the left compared to the symmetrical case, since the left travelling wave runs behind on the right running wave (due to the phase shift ϕ). In order to compensate for this delay, the distance covered by the left travelling wave must decrease and therefore the peak M2 tidal velocity current occurs for shorter basin length. The opposite occurs at the second entrance, where the right travelling wave must cover more distance, since it runs ahead of the left travelling wave (at entrance 2). Furthermore, for the non-symmetrical case, the M2 tidal velocity at entrance 2 is smaller than at entrance 1 for basin shallower than 20 m.

For the symmetrical case, the peak in the linearized friction coefficient coincides with the peak in the dimensionless current. This is in agreement with Eq. (2.12), since the highest amplitude of the M2 tidal velocity current causes the friction coefficient to maximize. When the non-symmetrical case is considered, it turns out that the peak of the linearized friction coefficient is still around $L_b/L_t = \pi$, but the peaks of the amplitude of the M2 tidal velocities currents have shifted. This also follows from Eq. (2.12). The friction coefficient contains integrals over x, since at the first entrance the peak current is for basins shorter than the tidal wavelength and the opposite is true for the second entrance. By taking the integral over the amplitude of the M2 tidal velocity (Eq. (2.12)), the net highest current over the channel will be found in between the two tidal velocity peaks and therefore around $L_b/L_t = \pi$.

Furthermore, since the symmetrical case consists of two waves of initially same amplitude and phase travelling in the opposite direction a standing wave is present for short basin. This is due to the fact that for short basins, the friction is weak and therefore almost no phase and amplitude shift occurs between the left and right running wave. Note that for a standing wave, the cosine of the phase difference between the tidal sea surface variation and the tidal velocity is zero. For a basin with the parameters of Table. 1 in the symmetrical case, the cosine of this phase difference is around -0.06 rad and therefore the M2 tidal wave is close to a standing wave. For the non-symmetrical case, this phase difference is around 0.81 rad and therefore no standing wave is present here. This behaviour becomes important when discussing the Stokes velocity in Subsection 5.3.

5.3 Tidal dynamics of M4 currents

The leading factors of the tidally averaged sediment import/export are $\cos(\phi_1 - 2\phi_0)$ and the amplitude of the M4 tidal velocity. For the sediment transport and the time evolution, the total phase shift and the total tidal velocity of the M4 tide are of importance, therefore no attention will be paid to the separate M4 tidal velocities (in Subsection 5.6, the sediment import/export of the separate M4 tidal components will be discussed). In Fig. 10, the dimensional amplitude of the total M4 tidal velocity is given for the symmetrical (left column) and non-symmetrical (right column) case at the first (top) and second (bottom) entrance.

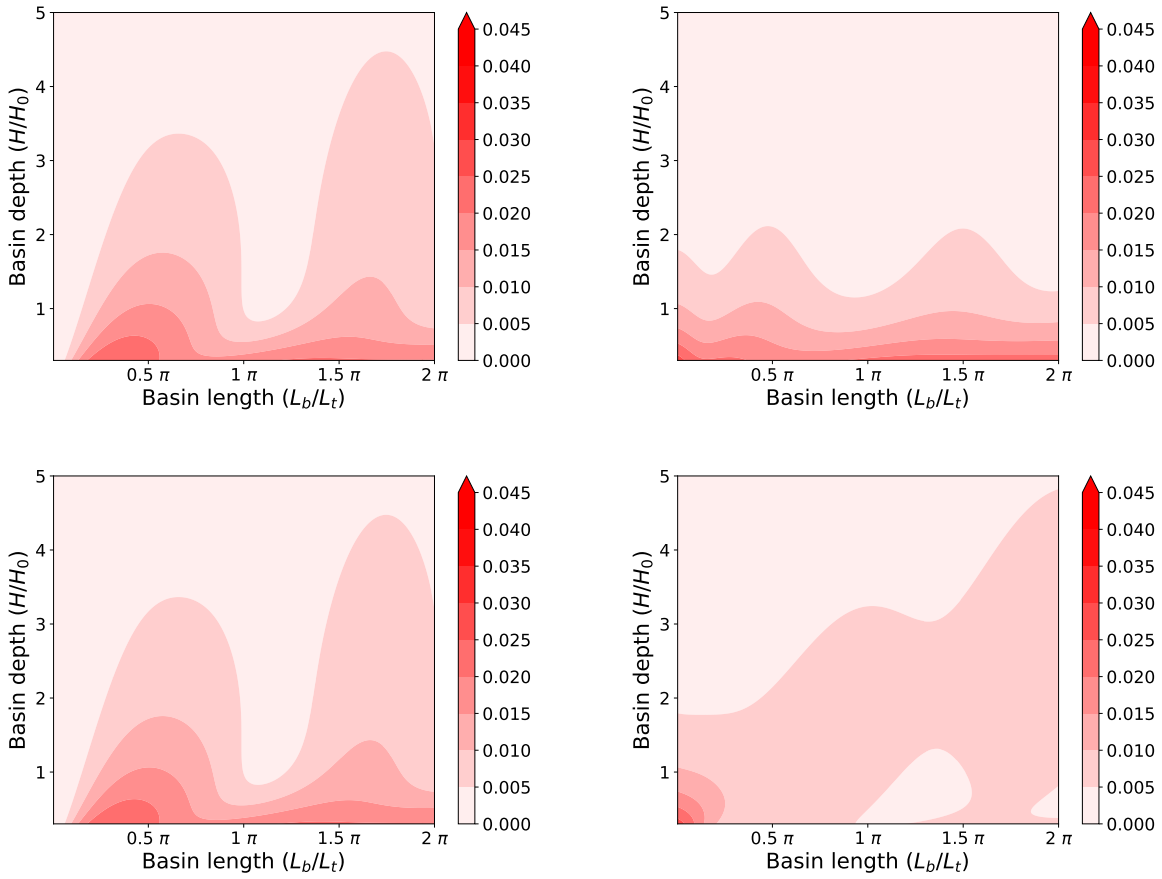

Figure 10: Colour plot of the dimensional amplitude of the total M4 tidal velocity (m/s) as a function of scaled basin depth H/H_0 and scaled basin length L_b/L_t. Here, the basin depth H is between 3 and 50 m and is scaled by $H_0 = 10$ m. The scaled basin length L_b/L_t is between 0.01 and 2π, where L_t ranges from 38.6 km for 3 m depth and 157.6 km for 50 m depth. The first row represents the first entrance and the second row gives entrance 2. The parameter values of Table. 1 are used.

For the symmetric and the non-symmetrical case, the dimensional amplitude of the total M4 tidal velocity decreases with increasing depth. In line with the dimensional M2 tidal velocity, the right panel of Fig. 10 (non-symmetrical case) shows that the dimensional total M4 tidal velocity at the second entrance is smaller compared to the first entrance for basins of less than 20 m depth. Furthermore, the dimensional M4 tidal velocity is an order two smaller than the dimensional M2 tidal velocity.

The cosine of the phase difference between the M2 and M4 current $\cos(\phi_1 - 2\phi_0)$ is the second important factor that determines the sediment import/export. For each situation (as before), this phase difference is shown for different basin sizes in Fig. 11. In this figure, the black line indicates when $\cos(\phi_1 - 2\phi_0) = 0$ and therefore the sign change.

For the symmetrical case, a clear standing wave pattern is observed with troughs near $\pi/2$ and $3\pi/2$ scaled basin lengths L_b/L_t and peaks near π and 2π. Furthermore, the asymmetry of the

symmetric case is also clearly visible. For non-symmetrical case, it is observed that the asymmetry is broken. For short basins (at $x = -\ell$) a region of negative values is observed, which is absent for the symmetric case. The same applies for positive values at the second entrance. When the two cases for the first entrance are compared, more or less the same behaviour is observed for large basin lengths. While for the second entrance a different pattern is shown. Here, the non-symmetrical case still has a positive sign for deep and long basin, which is not the case for the symmetrical case.

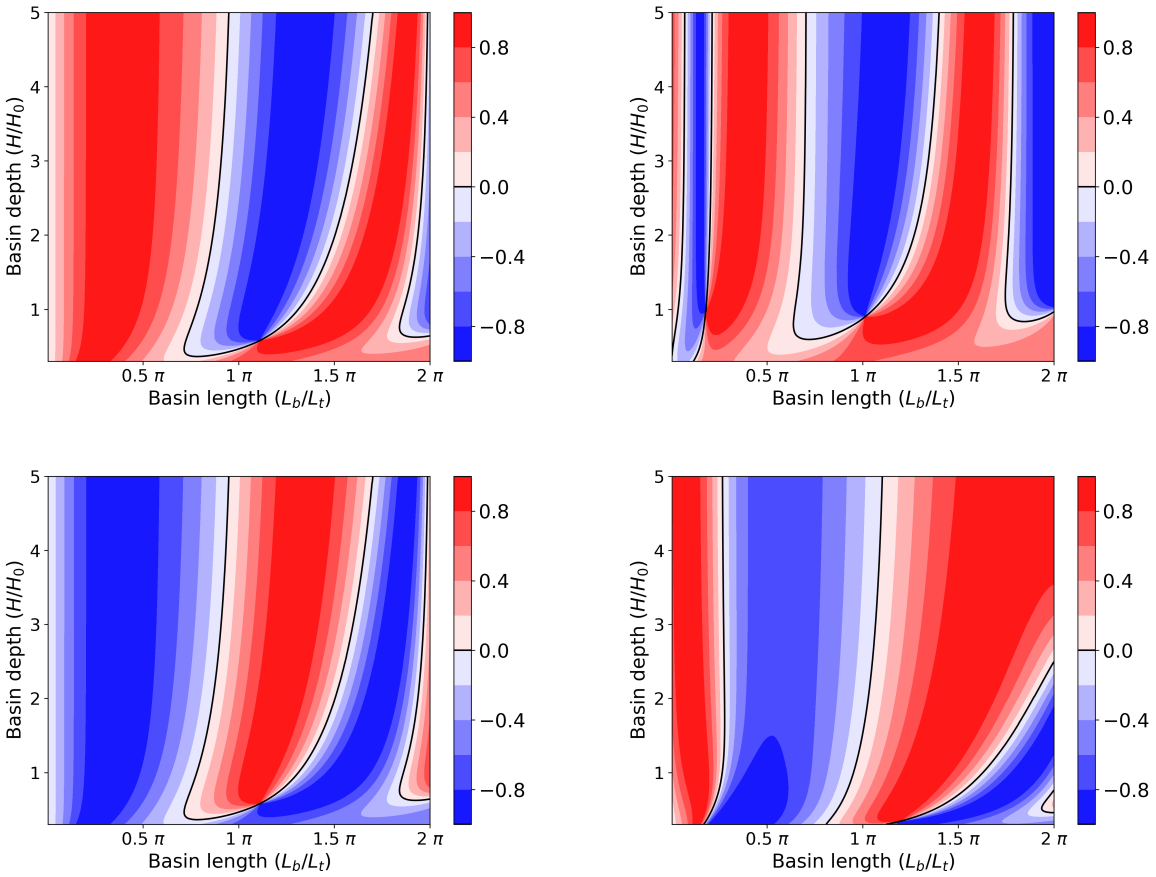

Figure 11: Colour plot of $\cos(\phi_1 - 2\phi_0)$, where ϕ_0 and ϕ_1 are the phase of the M2 current and the total M4 current as a function of scaled basin depth H/H_0 and scaled basin length L_b/L_t. Here, the basin depth H is between 3 and 50 m and is scaled by $H_0 = 10$ m. The scaled basin length L_b/L_t is between 0.01 and 2π, where L_t ranges from 38.6 km for 3 m depth and 157.6 km for 50 m depth. The black line indicates the zero line. The parameter values of Table. 1 are used.

5.4 Dynamics of tidal residual (M0) current

The residual current consists of a residual mass transport velocity ($u1m$) and a Stokes velocity (Section 3). In Fig. 12 the dimensionless residual current with these two components (without ϵ) are plotted in an along-channel view. Here, it is shown that for the symmetrical case, the Stokes velocity and the residual current are an order 1 smaller than the non-symmetrical case. For the symmetrical case, the M2 tide shows a near standing wave behaviour (see Subsection 5.2) for a basin with a length of 70 km, default values from Table. 1. For a full standing wave the net displacement of a

fluid parcel over one tidal cycle is in the vertical direction only (standing waves do not propagate). Therefore the Stokes velocity becomes near zero for the symmetrical case. For the non-symmetrical case, there is no standing (M2 tide) wave in the basin and therefore the net displacement of a fluid parcel over one tidal cycle is also directed in the direction of wave propagation, resulting in a much higher Stokes velocity for the non-symmetrical case compared to the symmetrical case.

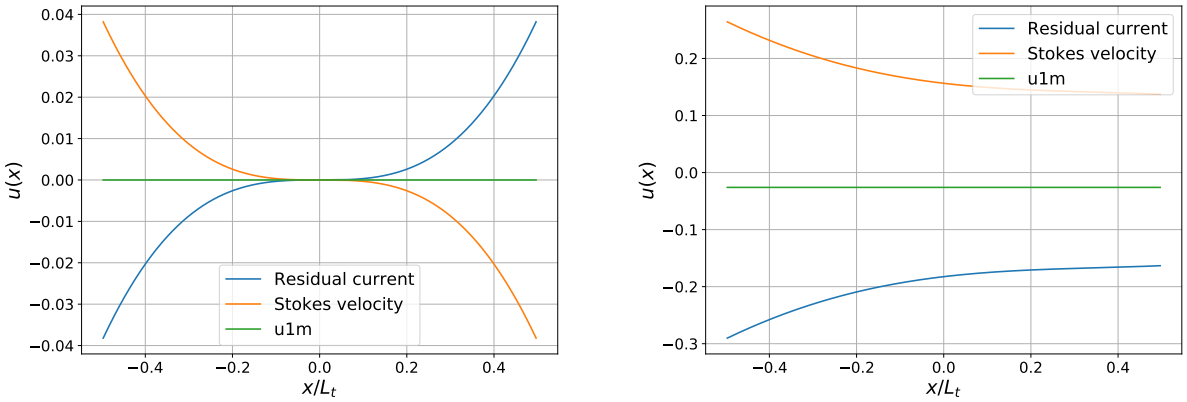

Figure 12: Along-channel view of the dimensionless residual current, through flow and Stokes velocity (without pre-factor ϵ) for the symmetrical case (left) and the non-symmetrical case (right) for a basin depth of 10 m and a basin length of 70 km. Here, the parameter values of Table 1 are used. The scaling parameter for the current is $U \approx 0.72$ m/s.

From Eq. (A.2), it follows that for the symmetrical case, the first two terms cancel each other and the integral will be zero for the residual mass transport velocity. Therefore, no through flow is expected here and thus the residual current and the Stokes velocity cancel each other (left panel of Fig. 12). For the non-symmetrical case (right panel of Fig. 12), these terms do not cancel or drop out and therefore a net through flow exists from the second to the first entrance (negative direction). Furthermore, it is shown that the Stokes velocity is always positive and the residual current is always negative, this also indicates a strong dependence on the values of α and ϕ since this behaviour is different from the symmetrical case.

Due to the constructive interference at entrance 2 and the destructive interference at entrance 1, the wave height at entrance 2 is always higher in case of the non-symmetrical channel. This results in a constant current between the two entrances, which is the residual mass transport velocity (as stated in Subsection 3.3). For the non-symmetrical case, it is observed that the amplitude of the tidal current and sea surface variation of the right travelling wave is greater than that of the left travelling wave (Figs. 8 and 21) for every location in the basin (since at both entrances, the right travelling wave is greater). Resulting in a non-negative Stokes velocity through the channel.

Similar to the M2 and M4 tidal currents, the dimensional residual tidal velocity for different basin lengths and depths is shown in Fig. 13. Similar to the M4 tidal velocity, in most regimes the residual current is much smaller than the M2 current. Furthermore, it is observed that for very short basins, the residual tidal velocity of the non-symmetrical case is much larger than the symmetrical case. Here, the tidal sea surface variation gradient between the two entrances is very large due to the short basin length, therefore resulting in a very large residual current. Furthermore, for long and

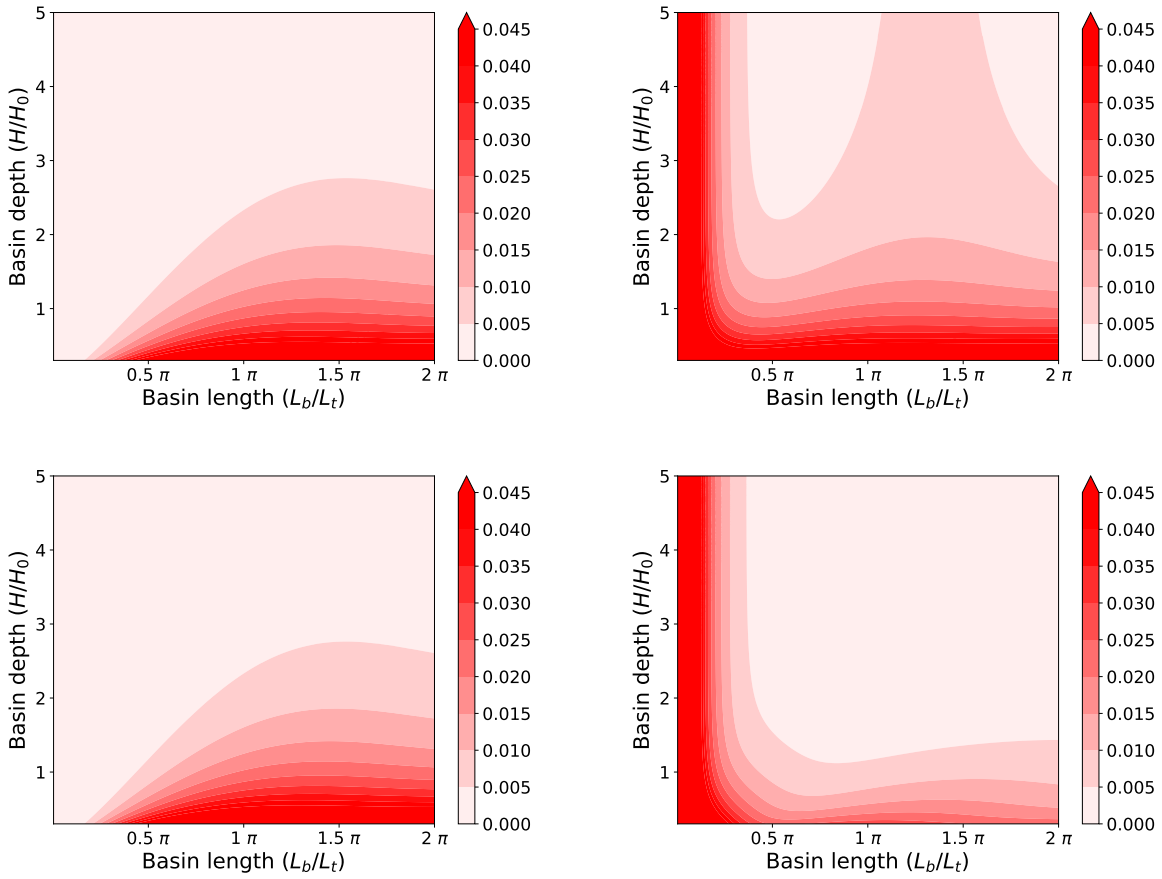

Figure 13: Colour plots of the dimensional amplitude of the residual current (m/s) as a function of scaled basin depth H/H_0 and scaled basin length L_b/L_t for the symmetrical (left panel) and the non-symmetrical (right panel) for the first entrance (top) and second entrance (bottom). Here, the basin depth H is between 3 and 50 m and is scaled by $H_0 = 10$ m. The scaled basin length L_b/L_t is between 0.01 and 2π, where L_t ranges from 38.6 km for 3 m depth and 157.6 km for 50 m depth.

shallow basins, the residual velocity at entrance 1 is for both cases around the same magnitude, while for the second entrance, the residual velocity for the non-symmetrical case is slightly smaller. When comparing the M4 and residual tidal velocities, it is observed that for short and shallow basins, the M0 current dominates over the M4 current. For longer and deeper basins, the M4 and residual current have similar magnitude.

5.5 Tidal current with M2, M4 and residual tide included

When the M2, M4 and M0 tides are included in the tidal dynamics of the system, the total tidal current will no longer be sinusoidal. Fig. 14 shows a time series (two tidal periods) of the tidal current that includes the M2, M4 and residual dimensionless tide for the symmetrical case for a basin with a length of 70 km and a depth of 10 m (see Table. 1 for parameter values). Due to the inclusion of the M4 and residual tides, the ebb current becomes larger than the flood current. Another asymmetry is also observed in the perturbed tide; the time from flood to ebb becomes shorter compared to the time from ebb to flood. Both asymmetries depend on the system settings

and therefore a larger flood current and/or a longer flood to ebb time is also possible.

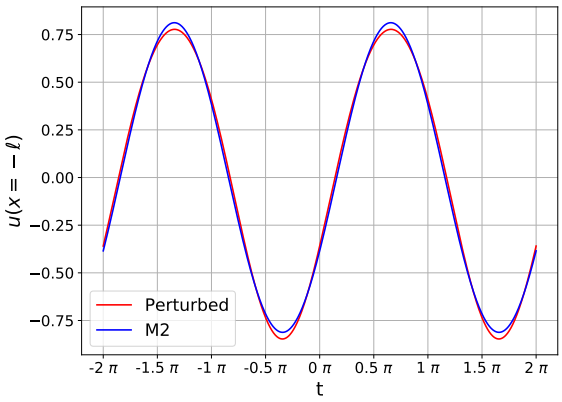

Figure 14: Times series of the dimensionless total tidal current, including the M2, M4 and residual tide for two tidal periods for the symmetrical case. Here, the default parameters of Table 1 are used with a depth of 10 m and a length of 70 km. The scaling parameter for the current is $U \approx 0.72$.

5.6 Net sediment import/export

Since the sediment transport rate is the driving factor behind the evolution of the basin, it is split up into the three separate non-linear tidal M4 components (given in Appendix B, Fig. B.2). For each M4 component, the dimensional net sediment import/export divided over the maximum sediment import/export $\langle q_{net} \rangle / \max(|\langle q_{net} \rangle|)$ is presented. Here, the pink/red region indicates sediment import and the blue region sediment export.

The first row of Fig. 15 represents the total M4 transport, the second row the M0 transport and the third row gives the total transport. For the total M4 transport in the symmetric case (left panel), it is observed that sign of the transport follows the pattern of the $\cos(\phi_1 - 2\phi_0)$ and that import occurs for very short basin and very long basins. Furthermore, export occurs for middle long basin. The sediment import/export is larger for shallow basins, which is in line with the higher tidal velocities in this regime compared to deeper basins. Stable and unstable equilibria exist. Note that an equilibrium exists when the net transport is equal to zero (black line). Two unstable equilibria (red on left, blue on right) and one stable equilibrium (blue on left, red on right) are observed. An unstable equilibrium occurs when the sediment import causes the basin to shrink, allowing it to import more sediments causing a positive feedback mechanism, by which the basin will fill up. The same principle applies for an unstable equilibrium where export occurs, the basin grows in size, which causes more export. The opposite occurs for a stable equilibrium. Here, when the basin shrinks in size, the export increases. This allows the basin to grow in size, meaning the basin will return to its equilibrium depth and length.

The non-symmetrical case (right panel) sediment transport shows similar behaviour, but with weaker sediment transport, due to the weaker current for the non-symmetrical (mimicking the Marsdiep-Vlie channel) case for a certain basin which is not too short. Furthermore, more areas are blue for the non-symmetrical case (compared to the symmetrical case) and therefore more export of sediment occurs.

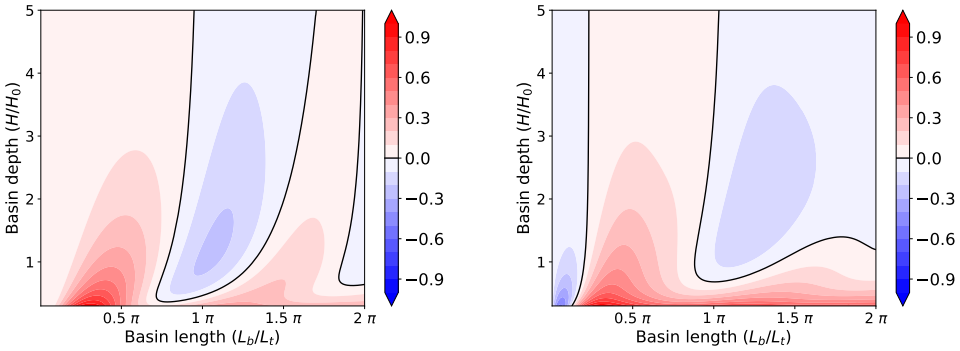

(a) $\max(|\langle q_{net}\rangle|) = 5.02 \cdot 10^{-5}\ m^2/s$ (b) $\max(|\langle q_{net}\rangle|) = 1.25 \cdot 10^{-5}\ m^2/s$

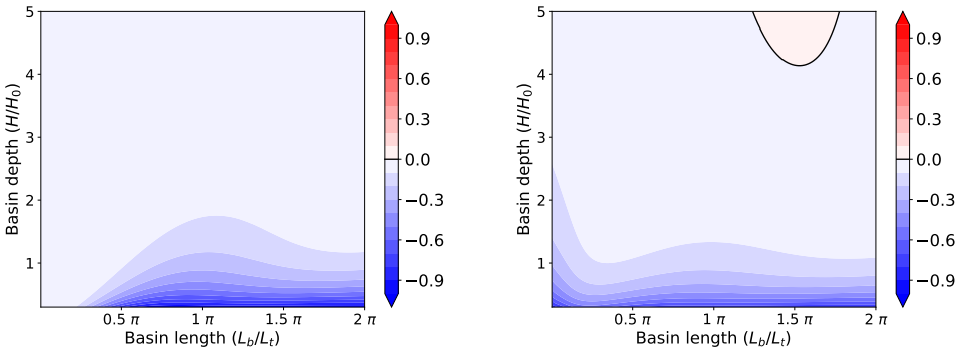

(c) $\max(|\langle q_{net}\rangle|) = 1.4 \cdot 10^{-4}\ m^2/s$ (d) $\max(|\langle q_{net}\rangle|) = 1.1 \cdot 10^{-4}\ m^2/s$

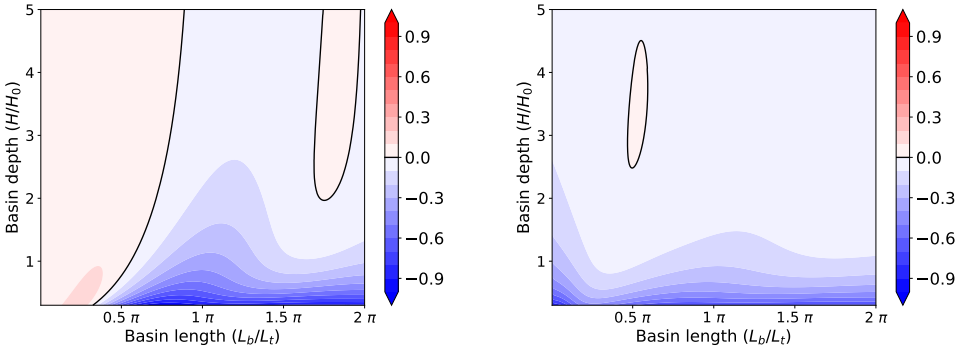

(e) $\max(|\langle q_{net}\rangle|) = 1.37 \cdot 10^{-4}\ m^2/s$ (f) $max(|\langle q_{net}\rangle|) = 1.05 \cdot 10^{-4}\ m^2/s$

Figure 15: Colour plots of the tidally averaged dimensional sediment transport (m^2/s) divided by the maximum of the absolute transport $\langle q_{net}\rangle / \max(|\langle q_{net}\rangle|)$ generated by the M4-current (first row), M0-current (second row) and these two tidal constituents combined (third row) for different basin lengths and depths for the symmetrical (left panel) and the non-symmetrical (right panel). Here, the basin depth H is between 3 and 50 m and is scaled by $H_0 = 10$ m. The scaled basin length L_b/L_t is between 0.01 and 2π, where L_t ranges from 38.6 km for 3 m depth and 157.6 km for 50 m depth. Furthermore, the parameter values of Table. 1 are used. For each subfigure $\max(|\langle q_{net}\rangle|)$ is given in the subcaption. Here, the pink/red region indicates sediment import and the blue region sediment export.

The total M4 transport consists of the transports due to the three non-linear forcing mechanisms (Appendix B, Fig. B.2). In Appendix B, it is shown that for the symmetrical case the excess mass flux and advection induced sediment transport rates are dominant over the friction for deeper basins. However, for shallow basin, the three components are of the same order of magnitude and the friction is slightly higher compared to the other two. When the asymmetrical case is considered, it is observed that the advection is slightly dominant over the excess mass flux and friction induced sediment transport. Here, the excess mass flux induced sediment transport is higher compared to the friction.

Next, the M0 current results only in export in the symmetrical case, while a small region of import exists for the non-symmetrical case. Furthermore, the sediment transport for very short basins of the non-symmetrical case shows a larger transport, which is in line with the large residual current in that regime.

For the time evolution of the basin, the total sediment transport (M4 and residual combined) is of importance. It is seen that in both cases, the maximum sediment transport of the residual tide is an order of magnitude higher compared to the M4. It is also observed that the sediment transport due to the residual tide is strong for shallow basin and weak for deep basins. Therefore, for shallow basins the residual tide induced sediment transport dominates over the M4. For short basins in the symmetrical case, the sediment transport induced by the total M4 tide dominates. For deeper, longer basins in the symmetrical case, the M4 current. For the asymmetrical case, the M4 tide dominates the residual tide for deep, long basins and for a small region of short, deep basins. However, for all other basin length and depths, the residual tide dominates.
When comparing the sediment transport of the symmetrical and asymmetrical case, it is evident that the values of α and ϕ are important for the sediment transport of the basin.

5.7 Time evolution of basin length and depth

In the previous subsections, the basin length L_b and depth H were used as if they were parameters, since no dependence on time was studied. However, since in this subsection their time evolution is presented, the basin length and depth becomes variables of state again and their initial value $H(t = 0)$ and $L_b(t = 0)$ are parameters. Mind that all figures are moved to the end of this subsection.

As mentioned in Section 4, four scenarios are studied to gain insight into the evolution of a basin with a certain initial length and depth. Experiment 1 (top row of Fig. 16 and 17) concerns the evolution without sea level rise and/or import by waves. Experiment 2 (bottom row of Fig. 16 and 17) includes the current day sea level rise. For experiment 3 (top row of Fig. 19 and 20) and experiment 4 (bottom row of Fig. 19 and 20) the import by waves is added using $q_{wave} = 0.04$, where for experiment 3 the current day sea level rise is considered, while for experiment 4 the sea level rise according to the RCP2.6 scenario is used. In the top row of Fig. 16, the black line indicates an equilibrium, since here the sediment transport is zero and no sea level rise present. For the second row of Fig. 16 and Fig. 19, the red line indicates that the sediment transport is zero, but due to sea level rise no equilibrium is present.

Fig. 16 shows the evolution of seven different initial basin depths and lengths for the symmetrical case (left column) and the non-symmetrical case (right column) with on the first row no sea level

rise and on the second row the current sea level rise. Special attention must be paid to the basin in the bottom left of the graph, the green line represents the symmetrical case (left panel) and the blue line the non-symmetrical case (right panel) for the initial condition of the channel mimicking the Marsdiep-Vlie channel (Table 1). Furthermore, Fig. 17 shows the time evolution of the length (left panel) and depth (right panel) of the symmetrical case (green line) and non-symmetrical case (blue line) for this initial condition.

First, the top rows of Figs. 16 and 17 (experiment 1) are considered. In the absence of sea level rise and sediment import by waves, it is observed that for the symmetrical case a short basin with initial conditions in the red region (import) fills up, while those in the blue region (export) tend towards a stable equilibrium. In Fig. 17 it is observed that for the symmetrical case, the initial condition mimicking the Marsdiep-Vlie channel fills up rapidly. When the non-symmetrical case is considered, it is observed that for almost all initial conditions export occurs and therefore lengthening and deepening of the basin. This also follows from the top row of Fig. 17, which reveals that for initial condition mimicking the Marsdiep-Vlie channel in the asymmetrical case the basin depth and length continue to deepen and lengthen.

Now, the second row is considered of Fig. 16 and 17. It is observed that for the symmetrical case, a deep basin with an initial condition in the import region starts to become deeper due to sea level rise. Furthermore, for initial condition in the export region, the pace of the deepening increases. Still, the basin mimicking the Marsdiep-Vlie channel fills up. Due to the added sea level rise, the filling up of the basin takes significantly longer (Fig. 17). When the asymmetrical case is considered, it is observed that the pace of the deepening of the basin increases due to sea level rise for all initial conditions. Do not be alarmed by the time evolution lines in the export part of the graph to move to shorter L_b/L_t (despite their being is export), since the basin length is scaled by $\sqrt{gH}\omega$ and H is increasing much faster than L_b, this means that L_b/L_t will decreases as is observed in Fig. 16. Now, consider in experiment 2 for both cases the initial condition of $H/H_0 = 1$ and $L_b/L_t = 3$ (fig. 16). It is observed that at first the dimensionless length ℓ increases, after which it decreases even though it remains in an export dominated state. The dimensional basin length L_b does always increase here and the behaviour of ℓ is due to the chosen scaling relation.

In Section 4, it was stated that due to the littoral drift along the Dutch coast, sediment is imported into the basin by waves $(q_{wave}) = 0.04$. A critical sea level rise can be defined as the sea level rise for which the depth of the basin does not change over time. The critical sea level rise must therefore be equal to the change of depth of Eq. 2.14 within one year. For both the symmetrical case and the asymmetrical case (left and right column respectively), the critical sea level rise is shown in Fig. 18.

For both cases, the region where the net sediment transport rate is negative, the critical sea level rise is also negative. So in order to keep the depth constant, the sea level must drop. For the symmetrical case, a high critical sea level rise is observed for very short basin of shallow depth. For all other basins sizes, the critical sea level rise is below the current sea level rise. When the asymmetrical case is considered, for short basins a very high export occurs, so the critical sea level rise must be negative there as well. Here too, for short shallow basins the critical sea level rise is large and for all other basin sizes it is below the current day sea level rise.

In Fig. 19, the evolution of the seven basins are considered with the inclusion of the sediment import by waves q_{wave}. This is performed for the current day sea level rise (experiment 3) and the sea level rise according to RCP2.6 scenario (experiment 4). In Fig. 20, the time evolution of the default

initial condition from Table. 1 is given for the symmetrical and non-symmetrical case with on the top row experiment 3 and on the bottom row experiment 4.

Due to the addition of the sediment import by waves, the sediment import/export of the asymmetrical case changes significantly. Now, for most region import occurs and a region of large export is observed for short basins. In Figs. 19 and 20, it is observed that the channel based on the parameter values of Table. 1, fills up for the symmetrical case for both experiments. When the non-symmetrical case is considered, different behaviour is observed between experiments 3 and 4. For experiment 3, the basin first decreases in depth and length (Fig. 20). When the basin becomes too short, it reaches the region of export for short basins, through which this initial condition starts to lengthen and deepen. For experiment 4, the sea level rise dominates over the tidal processes and the import by waves and all basin become deeper.

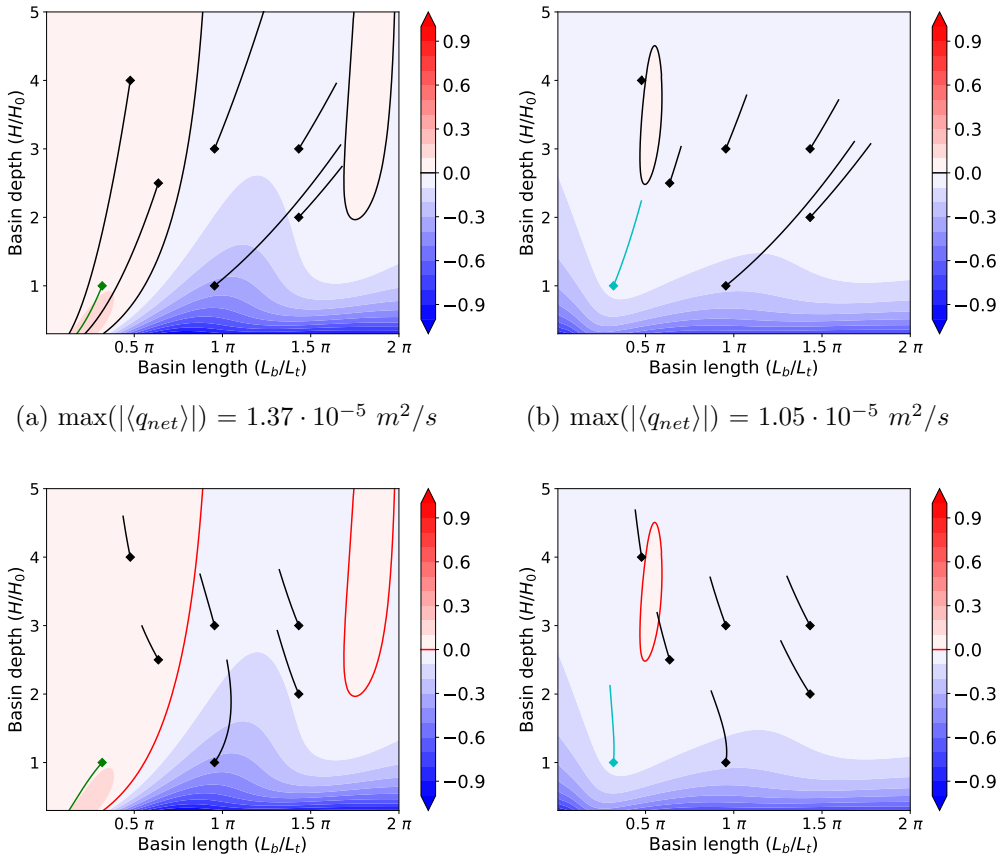

(a) $\max(|\langle q_{net}\rangle|) = 1.37 \cdot 10^{-5}\ m^2/s$

(b) $\max(|\langle q_{net}\rangle|) = 1.05 \cdot 10^{-5}\ m^2/s$

(c) $\max(|\langle q_{net}\rangle|) = 1.37 \cdot 10^{-4}\ m^2/s$

(d) $\max(|\langle q_{net}\rangle|) = 1.05 \cdot 10^{-4}\ m^2/s$

Figure 16: Colour plot showing the dimensionless evolution for seven different basin initial conditions under the symmetric case with no sea level rise (first row, over 100,000 yr) and the current day sea level rise (second row, over 4,000 yr). The second column gives the asymmetrical case. Here, the basin depth H is between 3 and 50 m and is scaled by $H_0 = 10$ m. The scaled basin length L_b/L_t is between 0.01 and 2π, where L_t ranges from 38.6 km for 3 m depth and 157.6 km for 50 m depth and the parameter values of Table 1 are used. The basin in the bottom left represents the initial condition mimicking the Marsdiep-Vlie channel. For the first row (first experiment), the black lines indicate equilibria, while for the second row (experiment 2), the red lines indicate where the transport is zero. Due to the sea level rise, the red lines are not equilibrium lines. The diamond shape indicates the initial depth and length. In the background, tidally averaged dimensional sediment transport (m^2/s) divided by the maximum of the absolute transport is given. For each case, the maximum transport is presented in the subcaptions.

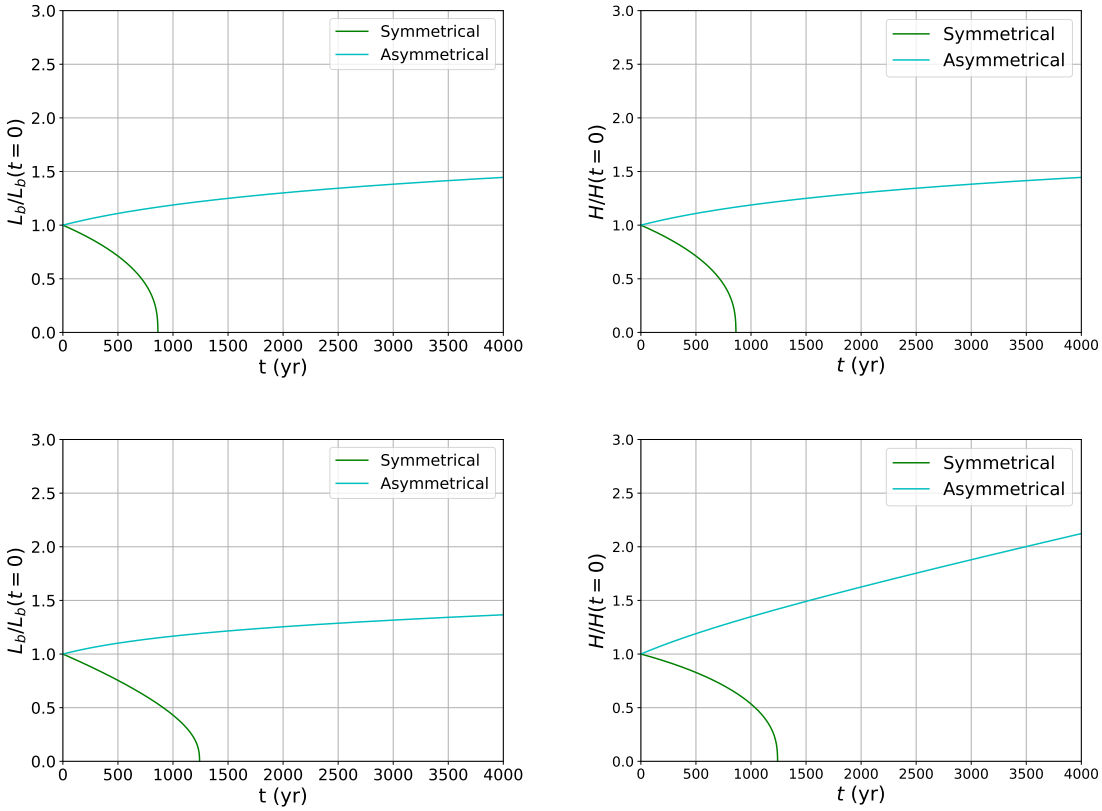

Figure 17: Time series in years of the evolution of the basin (mimicking the Marsdiep-Vlie channel) length divided over the initial length (left) and depth divided over the initial depth (right), based on the parameter values of Table. 1. The symmetrical case is given in green, while the asymmetrical case is given in blue. The top row represents experiment 1, while the bottom row represents experiment 2. For experiment 1, the first 4,000 years are shown.

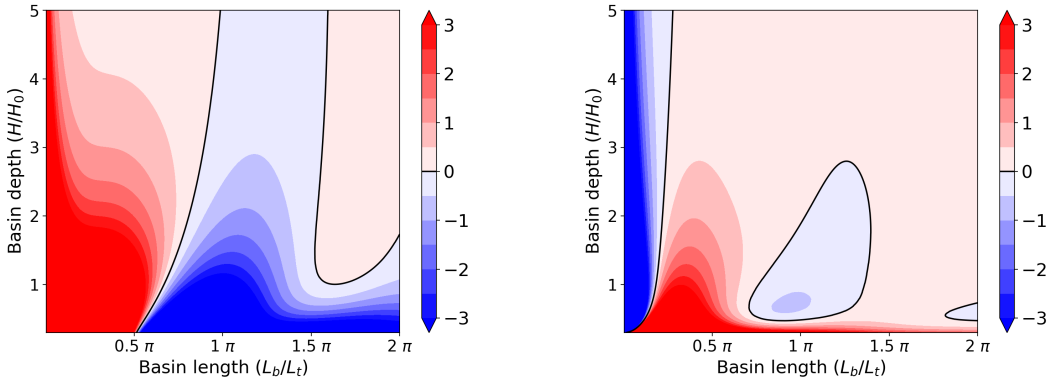

Figure 18: Colour plot showing the critical sea level rise for the symmetrical case (left) and the asymmetrical case (right) in mm/yr. Here, the basin depth H is between 3 and 50 m and is scaled by $H_0 = 10$ m. The scaled basin length L_b/L_t is between 0.01 and 2π, where L_t ranges from 38.6 km for 3 m depth and 157.6 km for 50 m depth and the parameter values of Table 1 are used. The import by waves is set to $q_{wave} = 0.04$. The black lines show a critical sea level rise of zero.

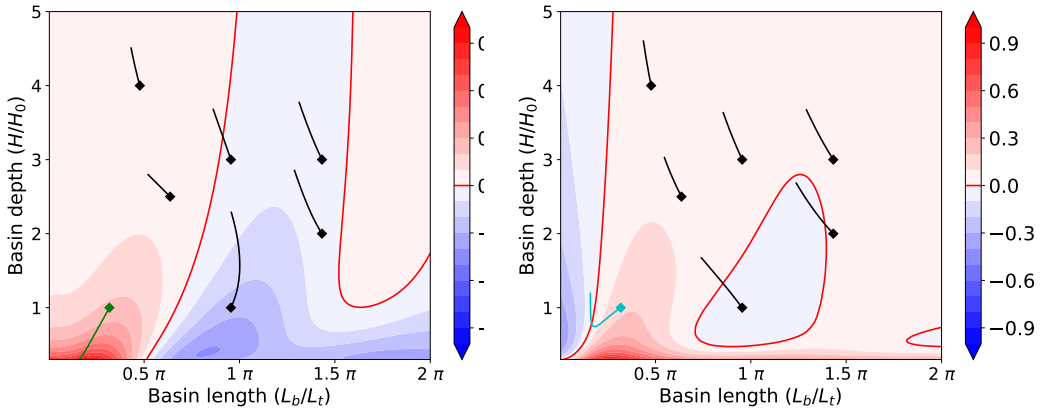

(a) $\max(|\langle q_{net}\rangle|) = 1.19 \cdot 10^{-4}\ m^2/s$ (b) $\max(|\langle q_{net}\rangle|) = 4.59 \cdot 10^{-5}\ m^2/s$

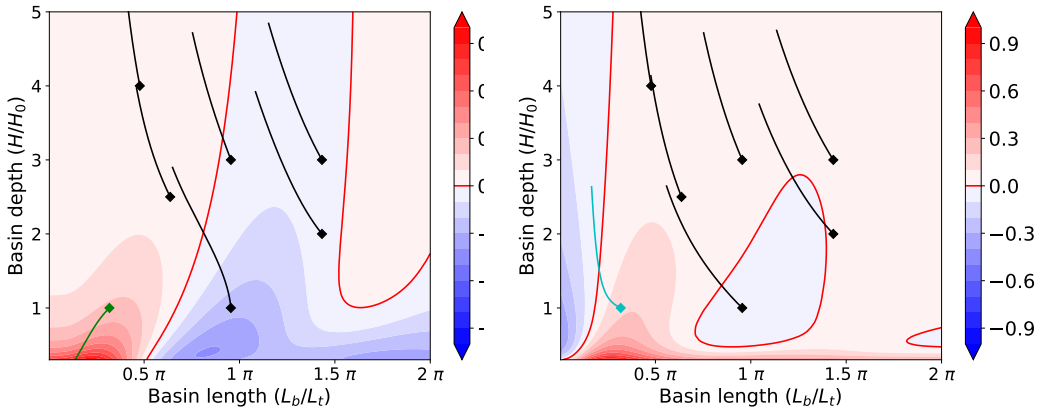

(c) $\max(|\langle q_{net}\rangle|) = 1.19 \cdot 10^{-4}\ m^2/s$ (d) $\max(|\langle q_{net}\rangle|) = 4.59 \cdot 10^{-5}\ m^2/s$

Figure 19: Colour plot showing the evolution dimensionless evolution for seven different basin initial conditions for experiment 3 (top row) and 4 (bottom row). The first column represents the symmetrical case and the second column the asymmetrical case. Here, the basin depth H is between 3 and 50 m and is scaled by $H_0 = 10$ m. The scaled basin length L_b/L_t is between 0.01 and 2π, where L_t ranges from 38.6 km for 3 m depth and 157.6 km for 50 m depth and the parameter values of Table 1 are used. The basin in the bottom left represents the initial condition mimicking the Marsdiep-Vlie channel. The red lines indicate where the transport is zero. Due to the sea level rise, the red lines are not equilibrium lines. The diamond shape indicates the initial depth and length. In the background, tidally averaged dimensional sediment transport (m^2/s) divided by the maximum of the absolute transport is given. For each case, the maximum transport is presented in the subcaptions.

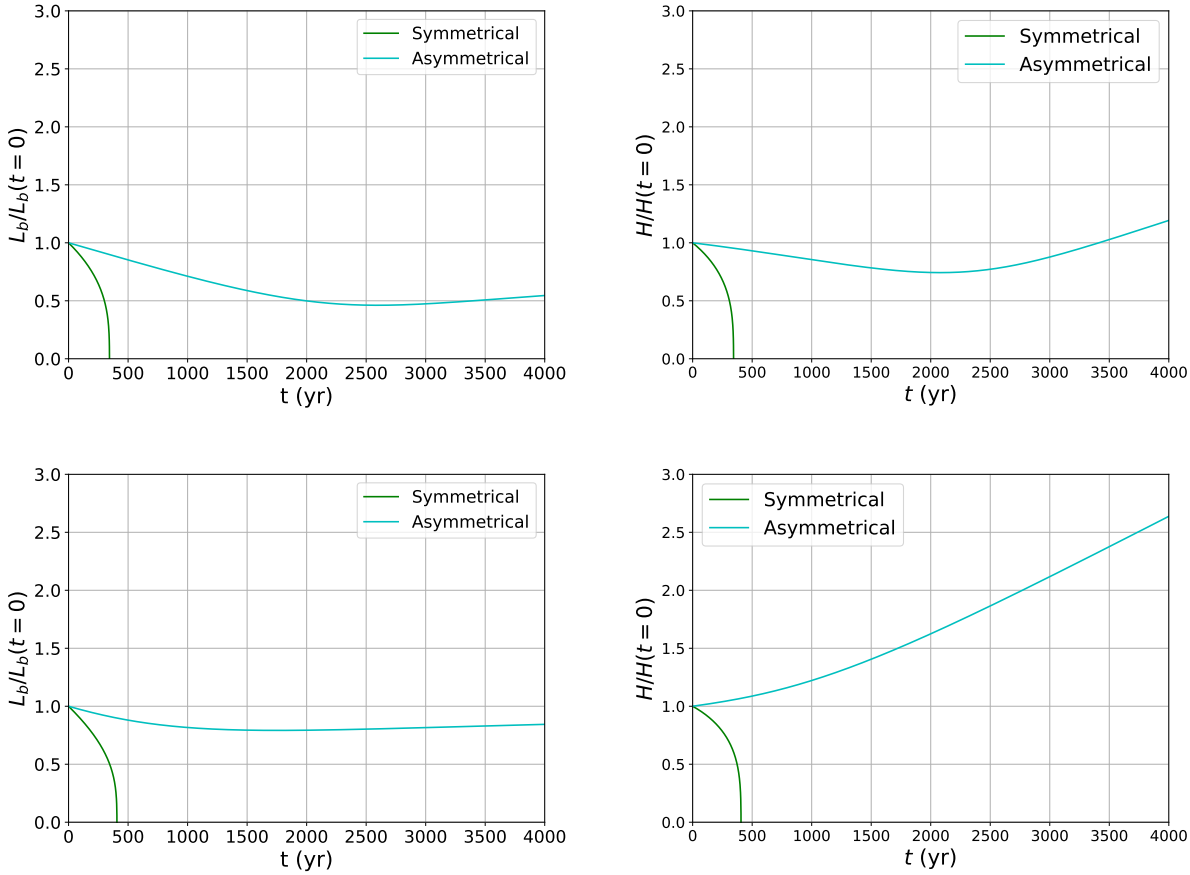

Figure 20: Time series in years of the evolution of the basin (mimicking the Marsdiep-Vlie channel) length divided over the initial length (left) and depth divided over the initial depth (right), based on the parameter values of Table. 1. The symmetrical case is given in green, while the asymmetrical case is given in blue. The top row represents experiment 3 and the bottom row represents experiment 4.

6 Discussion

The main findings of this research are summarized below. First, the internal generated residual and M4 tide are determining factors for the sediment import/export, since it leads to asymmetries in the dominant tide. Furthermore, it is shown that tidal current are not the only factor controlling the evolution, the littoral drift and therefore net import of sediment by waves changes the overall sediment import/export of the basin (especially for the asymmetrical case). Sea level rise can force a basin to move away from its equilibrium size and therefore changing its evolution. Using the two case studies (symmetric and non-symmetric), it is shown that the hydrodynamics and the evolution of such a channel strongly depends on the amplitude and phase shift of the incoming tidal wave between the entrances.

Interest is in the differences in results between this model and the one presented by *Frankemölle* (2020). As mentioned earlier, when the symmetrical case is considered, half of the basin effectively becomes the basin studied by *Frankemölle* (2020) with radiative damping. Radiative damping is a leakage of energy in the system, therefore the dominant (M2) tidal velocity decreases due to it. When the sediment transport induced by the M4 and residual is considered, it is also shown that due to radiative damping the transport decreases significantly. This is also reflected in the time evolution, which in this study happens much slower. Overall, the the symmetrical case of this study and the model of *Frankemölle* (2020) show the same behaviour but with different magnitudes.

The effects of making the channel asymmetric are considered by comparing the asymmetrical case with *Frankemölle* (2020). A major difference between the two studies is the residual current for short basins. In the study of *Frankemölle* (2020), the residual tidal velocity is small, while in this model it can become large due to the existing pressure gradient between the two entrances. In this study, the sediment transport of the M4 and residual tide (and therefore the combined tide) is significantly different from the one observed by *Frankemölle* (2020). Due to the weaker sediment transport (of both cases), both the import by waves and the sea level rise have a much greater effect on this model compared to a single inlet. In general, the effects of an asymmetric tide and thus those of a channel with two entrances (compared to a single inlet) are profound.

The main goal of this study is primarily to gain insight into the (tidal) processes that govern the evolution of a channel with two entrances. A direct comparison between the evolution of the default channel (mimicking the Marsdiep-Vlie channel) and existing literature is not possible, due to many differences between the strongly simplified channel of this model and the actual Marsdiep-Vlie system. For example: according to this model, the default channel will drown under the RCP2.6 scenario. Existing studies on the evolution of the Wadden Sea are performed by *Wang et al.* (2018) and *Van der Spek* (2018). Both these studies found that the Wadden Sea in the RCP2.6 projection will not drown.

Here, the main differences between the channel in this model and the Marsdiep-Vlie system are highlighted. First, the model does not have tidal inlets, instead it consists of two entrances. Secondly, tidal flats are absent in this model. However, tidal flats have an influence on the sediment transport (*Speer and Aubrey*, 1985) and therefore should be taken into consideration. Next, from Fig. 1 (*Elias et al.*, 2012) it follows that the depth decreases when moving further into the basin, and is close to zero near the water divide. This is significantly different from the homogeneous depth used in this model. Another major simplification concerns the assumptions that all imported/exported sediment deposits/erodes homogeneously and that the sediment import/export at

the two entrances is leading for the total import/export. Both do not occur in reality and should differ per location in the basin. The equation for the sediment transport rate is also simplified, since it is only a simple relation using the current cubed times a constant and processes like settling lags are not taken into account. Furthermore, atmospheric effects and discharge of fresh water from for example the IJsselmeer (*Duran-Matute et al.*, 2014) are not integrated into this model. When the time evolution is considered, the incoming tidal wave height Z and phase difference ϕ should be function of sea level rise, which has not been taken into account in this study. Lastly, an external M4 tide is neglected, however the amplitude of the M4 tide on the North Sea near the Wadden Sea is around 0.1-0.15 m, estimated from *Sinha and Pingree* (1997), and is therefore not negligible.

As described in the previous part of this section, the model consists of many simplifications. In the following part, some improvements are proposed for future research. The first improvement can be obtained by adding an external M4-tide, for reasons mentioned before. A second improvement can be made by adding a bottom slope to the model (e.g. (*Prandle and Rahman*, 1980; *Schuttelaars and de Swart*, 1997)). A linear bottom slope would be the simplest bottom improvement to the model. Furthermore, a local sediment transport should be defined (instead of one where sediment transport at the two entrances is leading). Such a model is presented by *Schuttelaars and de Swart* (1997) and allows for a more realistic sediment transport.

Now, some attention must be paid to the time evolution equation for the length of the basin. In this study, it is assumed that the eroded sediments spreads out homogeneously after leaving the basin and that the two entrances remain at the same location in time (fixed value for α and ϕ). The latter implies that the morphological changes (channel becomes deeper/shallow and shorter/longer) occur in the back-barrier in basin. This assumption is based on the Marsdiep-Vlie channel, which is not a straight channel, where deposition/erosion can occur in the channel bends and therefore changing its length. For the increase in length of a straight channel however, deposition must take place in the sea/ocean at the outer edge of the channel, since there are no channel bends. When a volume sediment is eroded from the channel, a part of it deposits at the outer edge of the entrances. Then, the amount of lengthening of the channel is the total deposited volume divided over the difference in depth between the sea and the channel. So, when erosion occurs, the depth of the outer region (sea/ocean) also becomes an important parameter for determining the change in length of the basin. This can also be taken into account in future research. However, this also implies that α and ϕ become time-dependent and therefore making the model more complex.

When import of sediments occur, the same assumptions as above were used. However, when a straight channel is considered, the imported sediment should only contribute to changes in depth. This is due to the fact that the depth must stay homogeneous and therefore the sediment is piled up layer on layer and thus not changing the length of the basin. Otherwise, the channel would be closed at some location. Here, the same consideration as above was used, that the channel mimics a back-barrier region. Furthermore, note that the time evolution equations Eqs. (3.29) are dependent on the fraction coefficient a, therefore gaining insight into sensitivity of the model with respect to this coefficient is of importance.

Now, attention must be briefly paid to how the perturbation theory is constrcuted. In this study x and u are scaled by H. When the basin is shallow and therefore H is small, this also results in value for ϵ close to 1. Since perturbation theory is based on a $\epsilon \ll 1$, one can say that they perturbation theory fails for very shallow basins. This is based on the subjective assumption that ϵ is not much smaller than 1 in that regime. Therefore, in future research a constant depth H_0 can be used for the

scaling relation for x and u and for appropriate H_0, ϵ will be much smaller than 1 for all basin depths.

Another topic of research is to study how strong the system depends on α and ϕ. In most of this study, the hydrodynamical and morphological equations for different basin lengths and depths were used, while for α and ϕ only two cases were chosen. As stated earlier, the tidal processes change significantly by altering α and ϕ. Examining the sensitivity of the model for different initial phase and amplitude shift can therefore be an interesting topic.

To conclude this discussion, one might think that this model is too simplistic due the mentioned simplifications and assumptions. Indeed, this model does not fully represent the reality, however the intriguing and fascinating side of this model is that it allows to study the processes occurring in a open channel. This model should not be used to determine a realistic basin evolution for a certain basin. However, it does provide the physical insight in the processes occurring in such a open channel system and can therefore be used as a toy-model in further research.

7 Conclusions

The primary aim of this study is to gain insight into the morphological evolution of a open channel system with and without the influence of sea level rise. As a secondary goal, the hydrodynamics and sediment transport in the channel was considered. This study is performed using a symmetrical and an asymmetrical case (mimicking the Marsdiep-Vlie channel) (Table.2).

For the evolution of the basin, it is found that without sea level rise, initial short basins in the symmetrical case fill up, while initial longer basins often tend towards a stable equilibrium. For the asymmetric case, most of the initial basins become deeper and longer over time, without finding an equilibrium. When sea level rise is added, deeper basins where import occurs cannot keep up with the sea level rise and will therefore drown in the symmetrical case. In the asymmetrical case, the drowning of the initial basin is accelerated. When a sediment import by waves is introduced, no differences are found for the symmetrical case. However, for the asymmetrical case most initial basins exhibit import instead of export. Still, the import of sediment is not able to compensate for sea level rise.

When the hydrodynamics and the associated sediment transport is considered, it is found that due to non-linear interactions in the basin, a residual tide and M4 overtides are generated. The latter consists of three contributions, namely advection, excess mass flux and friction. When these two tidal constituents are super positioned on the dominant (sinusoidal) M2 tide, the resulting tide becomes slightly asymmetric, resulting in a net sediment transport. It is found that for the symmetrical case the M4 tide is dominant for shorter basins, while for longer, shallower basins the residual tide is dominant. For the asymmetrical case, the residual tide is primarily dominant as a result from tidal sea surface variation differences between the two entrances.

A Appendix A

A.1 Solution for through flow

Here, the solution for the through flow/residual mass transport velocity (Eq. (A.1) is obtained. When integrating Eq. (3.19a), the following equation is obtained:

$$\bar{u} + \underbrace{\frac{1}{4}\hat{u}_0\hat{\eta}_0^* + \frac{1}{4}\hat{u}_0^*\hat{\eta}_0}_{\text{Stokes velocity}} = \underbrace{\bar{u}_{1m}}_{\text{Through flow}} .$$

With help of the Eq. (A.1), the second differential equation (Eq. (3.19b)) is rewritten as

$$\frac{d}{dx}[\bar{\eta} + \frac{1}{4}\hat{u}_0\hat{u}_0^*] = \frac{\lambda}{2}[\hat{u}_0\hat{\eta}_0^* + \hat{u}_0^*\hat{\eta}_0] - \lambda\bar{u}. \tag{A.1}$$

It follows from Eq. (A.1) that when the through flow is known, also the residual current is known because the stokes drift depends only on the zeroth order solution. Therefore, Eq. (A.1) and the corresponding boundary condition (Eq. (3.20)) are used to find an expression for the through flow. Eq. (A.1) is integrated once and then the boundary conditions on $x = \pm\ell$ are used. This gives a through flow given by

$$\bar{u}_{1m} = \frac{1}{8\ell\lambda}[\hat{u}_0\hat{u}_0^*]_{x=-\ell} - \frac{1}{8\ell\lambda}[\hat{u}_0\hat{u}_0^*]_{x=\ell} + \frac{1}{4\ell}\int_{-\ell}^{\ell} \hat{u}_0\hat{\eta}_0^* + \hat{u}_0^*\hat{\eta}_0 dx. \tag{A.2}$$

The residual current is then obtained by inserting equation A.2 into equation A.1.

A.2 Solution first overtide

The governing equation for the first overtide is given by

$$\frac{1}{2}\frac{d^2\hat{\eta}_1}{dx^2} + \kappa_1^2\hat{\eta}_1 = \underbrace{-\frac{i}{2}\frac{d}{dx}[\hat{u}_0\hat{\eta}_0}_{\text{Excess mass flux}}] + \underbrace{\frac{\lambda}{2}\frac{d}{dx}[\hat{u}_0\hat{\eta}_0]}_{\text{Friction}} - \underbrace{\frac{1}{4}\frac{d}{dx}[\hat{u}_0\frac{d}{dx}\hat{u}_0]}_{\text{Advective}} \tag{A.3}$$

where

$$\kappa_1 = \sqrt{2 + i\lambda}. \tag{A.4}$$

With the corresponding the boundary conditions A.5:

$$\hat{\eta}_1^{in}(x = -\ell) = \hat{\eta}_1^{in}(x = \ell) = 0. \tag{A.5}$$

As mentioned in section 3, equation A.3 has three non-linear forcing terms, namely advection, excess mass flux and friction. Therefore, equation A.3 is solved by treating each non-linear forcing term separately and thus resulting into three separate differential equations to solve. Since the method of solving these equations is the same, a general method is treated using a generalized forcing term $f(x)$. The generalized differential equation for the forcing terms then becomes

$$\frac{d^2\hat{\eta}_1^{f(x)}}{dx^2} + \kappa_2^2\hat{\eta}_1^{f(x)} = f(x). \tag{A.6}$$

Where $\kappa_2 = \sqrt{2}\kappa_1$. Equation A.6 is a forced harmonic oscillator and therefore a particular and a homogeneous solution exists. As mentioned before, the only interest is in the particular solution. In order to solve equation A.6, the following ansatz is made:

$$\hat{\eta}_1^{f(x)} = A^{f(x)}(x)e^{i\kappa_2 x} + B^{f(x)}(x)e^{-i\kappa_2 x}. \tag{A.7}$$

Here $A^{f(x)}(x)$ and $B^{f(x)}(x)$ are integration constant. Using this ansatz in equation A.6, and following the method presented by *Frankemölle* (2020), the following expressions are obtained for the integration constants

$$\frac{dA^{f(x)}(x)}{dx} = -\frac{i}{2\kappa_2}e^{-i\kappa_2 x}f(x), \tag{A.8}$$

$$\frac{dB^{f(x)}(x)}{dx} = \frac{i}{2\kappa_2}e^{i\kappa_2 x}f(x). \tag{A.9}$$

Equations A.8 and A.9 are integrated to obtain solutions for $A^{f(x)}(x)$ and $B^{f(x)}(x)$. Since equation A.8 concerns the right travelling part of the full solution, it is integrated from $x' = -\ell$ to $x' = x$ and using the boundary condition (eq. A.5) at $x' = -\ell$, where x' is a dummy variable to be integrated over. In the same manner equation A.9 is integrated from $x' = \ell$ to $x' = x$ and using the boundary condition (eq. A.5) at $x' = \ell$, since here the left travelling wave is evaluated.

Solving these integrals give expressions for $A^{f(x)}(x)$ and $B^{f(x)}(x)$, which together with equation A.7 gives the full solution of $\hat{\eta}_1^{f(x)}$.

As mentioned in the theory, for the sediment transport rate the currents of the first overtide must be known. To do so the momentum equation (eq. 3.22a) for the first overtides is used. For convenience, this equation is re-stated below

$$-i\hat{u}_1 + \frac{1}{4}\hat{u}_0\frac{d}{dx}\hat{u}_0 = -\frac{1}{2}\frac{d}{dx}\hat{\eta}_1 + \frac{\lambda}{4}\hat{u}_0\hat{\eta}_0 - \frac{\lambda}{2}\hat{u}_1.$$

As mentioned earlier, the momentum equation consists of two non-linear forcing terms in zeroth order. For each case (advection, excess mass flux and friction) the corresponding term from the momentum equation can be picked and used to solve for the corresponding overtide current. This results in three equations, one for each overtide

$$\begin{aligned}
\hat{u}_1^{EMF} &= \frac{1}{-2i+\lambda}\left(\frac{1}{2}\frac{d}{dx}\hat{\eta}_1^{EMF}\right), \\
\hat{u}_1^{ADV} &= \frac{1}{-2i+\lambda}\left(\frac{1}{2}\frac{d}{dx}\hat{\eta}_1^{ADV} + \frac{1}{4}\hat{u}_0\frac{d}{dx}\hat{u}_0\right), \\
\hat{u}_1^{Fr} &= \frac{1}{-2i+\lambda}\left(\frac{1}{2}\frac{d}{dx}\hat{\eta}_1^{Fr} + \frac{\lambda}{4}\hat{u}_0\hat{\eta}_0\right).
\end{aligned} \tag{A.10}$$

Using these three equations, the current of the first overtide for the advective, excess mass flux and friction are obtained.

B Appendix B

B.1 Dimensionless sea surface variation

In this appendix, four plots are giving where the dimensionless left travelling, right travelling and the total sea level deviation of the M2-wave is presented for a depth of 10 m and a length of 70 km for the two cases at each entrance.

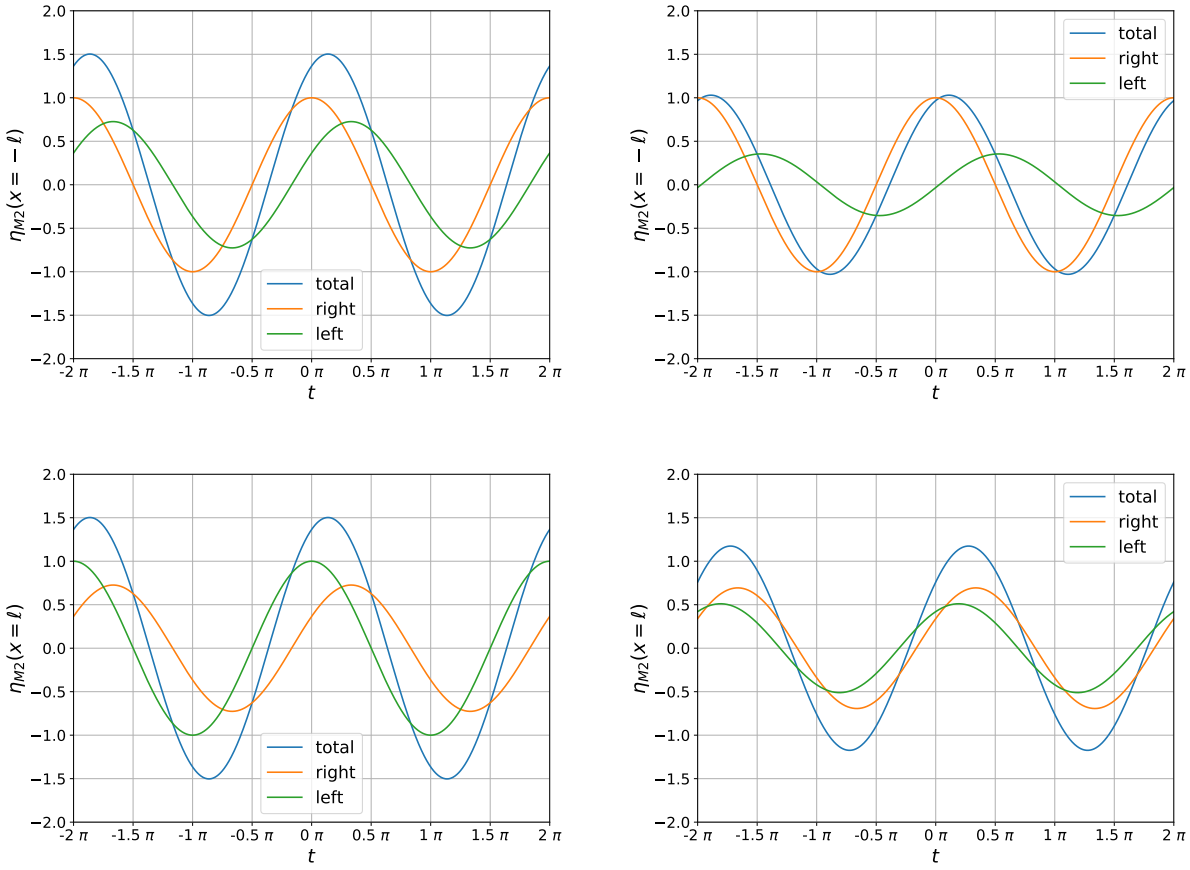

Figure 21: Time series of the dimensionless dominant tidal sea surface variation for a basin of 10 m depth and a length of 70 km for the symmetric (first column) and non-symmetric (second column) for two tidal periods. The first row represents the first entrance and the second row gives entrance 2. The scaling relation for the tidal sea surface variation is $\eta \approx 0.73$ and the parameters from Table. 1 are used.

B.2 Dimensional sediment transport rate due to the three M4 components

In this appendix, the dimensional net sediment transport divided over the maximum sediment transport due to the three non-linear components of the M4-current are presented for both cases.

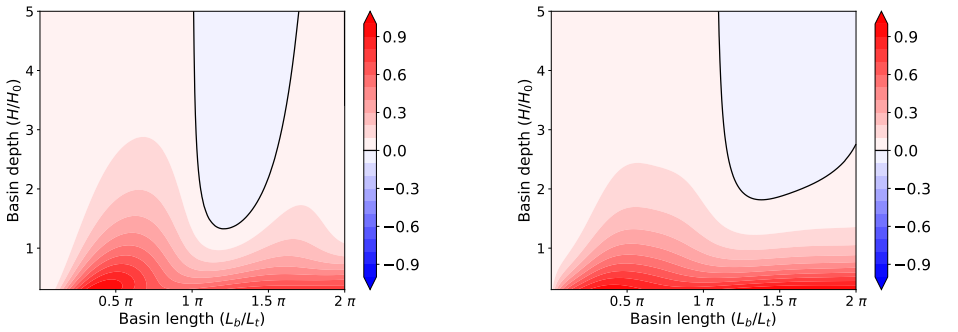

(a) $\max(|\langle q_{net}\rangle|) = 2.29 \cdot 10^{-5}\ m^2/s$ (b) $\max(|\langle q_{net}\rangle|) = 1.09 \cdot 10^{-5}\ m^2/s$

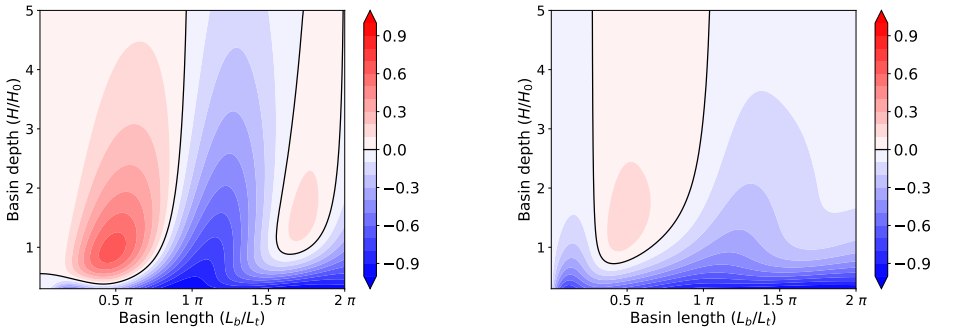

(c) $\max(|\langle q_{net}\rangle|) = 1.45 \cdot 10^{-5}\ m^2/s$ (d) $\max(|\langle q_{net}\rangle|) = 8.85 \cdot 10^{-6}\ m^2/s$

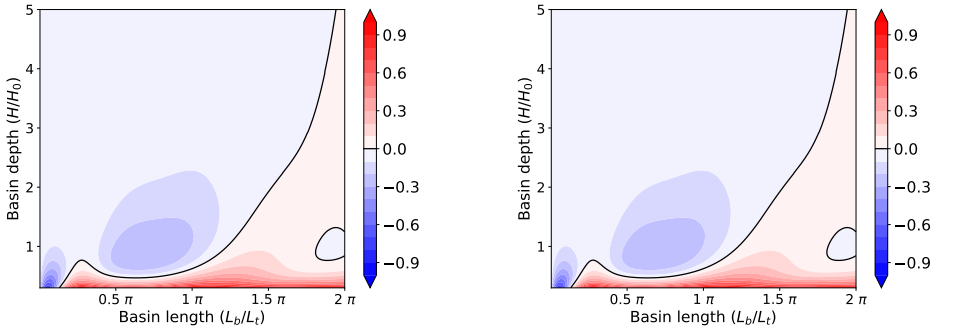

(e) $\max(|\langle q_{net}\rangle|) = 3.74 \cdot 10^{-5}\ m^2/s$ (f) $\max(|\langle q_{net}\rangle|) = 7.24 \cdot 10^{-6}\ m^2/s$

Figure 22: Colour plots of the tidally averaged dimensional sediment transport (m^2/s) divided by the maximum of the absolute transport $\langle q_{net}\rangle / \max(|\langle q_{net}\rangle|)$ generated by advection (first row), excess mass flux (second row) and friction (third row) for different basin lengths and depths for the symmetrical (left panel) and the non-symmetrical (right panel). Here, the basin depth H is between 3 and 50 m and is scaled by $H_0 = 10$ m. The scaled basin length L_b/L_t is between 0.01 and 2π, where L_t ranges from 38.6 km for 3 m depth and 157.6 km for 50 m depth. The parameters from Table 1 are used. For each subfigure $max(|\langle q_{net}\rangle|)$ is given in the subcaption.

References

Bagnold, R. A., The Nature of Saltation and of 'Bed-Load' Transport in Water, *Proceedings of the Royal Society of London. Series A, Mathematical and Physical Sciences*, *332*, 473 – 504, 1973.

CBS, 1,3 miljoen toeristen op vakantie naar de Wadden, 2016.

Church, J. A., P. U. Clark, A. Cazenave, J. M. Gregory, S. Jevrejeva, A. Levermann, M. A. Merrifield, G. A. Milne, R. S. Nerem, P. D. Nunn, A. J. Payne, D. Stammer, P. W. T, and A. S. Unnikrishnan, Sea level change. in: Climate change 2013: The physical science basis. contribution of working group i to the Fifth Assessment Report of the Intergovernmental Panel on Climate Change, 2013.

Davis Jr., R. A., and D. M. Fitzgerald, *Beaches and Coasts*, John Wiley & Sons Ltd, 2020.

Dissanayake, D. M. P. K., R. Ranasinghe, and J. A. Roelvink, The morphological response of large tidal inlet/basin systems to relative sea level rise., *Climatic Change*, pp. 253–276, doi: https://doi-org.tudelft.idm.oclc.org/10.1007/s10584-012-0402-z, 2012.

Duran-Matute, M., T. Gerkema, G. J. de Boer, J. J. Nauw, and U. Gräwe, Residual circulation and freshwater transport in the Dutch Wadden Sea: a numerical modelling study, *Ocean Science*, *10*(4), 611–632, doi:10.5194/os-10-611-2014, 2014.

Elias, E. P. L., A. J. F. van der Spek, Z. B. Wang, and J. de Ronde, Morphodynamic development and sediment budget of the Dutch Wadden Sea over the last century, *Netherlands Journal of Geosciences - Geologie en Mijnbouw*, *91*(3), 293–310, doi:10.1017/S0016774600000457, 2012.

Frankemölle, P. F. V. W., Analyzing time evolution of a tidal inlet due to nonlinear tides, sea level rise and waves with an idealised model (Bachelor thesis), 2020.

Gerkema, T., *Tides in Coastal Seas and Basins*, p. 122–156, Cambridge University Press, doi: 10.1017/9781316998793.007, 2019.

Lorentz, H. A., Verslag Staatcommissie Zuiderzee, *Algemene Staatsdrukkerij*, 1926.

Parker, B. B., The relative importance of the various nonlinear mechanisms in a wide range of tidal interactions (review), *Tidal Hydrodynamics*, 1991.

Plüß, A., North-Sea Model of the BAW: Simulation of Tidal Dynamics in the North-Sea with focus on the German Bight, *Die Küste*, *67*, 83 – 127, 2003.

Prandle, D., and M. Rahman, Tidal response in estuaries, *Journal of Physical Oceanography*, *10*(10), 1552 – 1573, doi:10.1175/1520-0485(1980)010⟨1552:TRIE⟩2.0.CO;2, 1980.

Ridderinkhof, W., H. E. de Swart, M. van der Vegt, N. C. Alebregtse, and P. Hoekstra, Geometry of tidal inlet systems: A key factor for the net sediment transport in tidal inlets, *Journal of Geophysical Research: Oceans*, *119*(10), 6988–7006, doi:https://doi.org/10.1002/2014JC010226, 2014.

Schuttelaars, H. M., and H. E. de Swart, An idealized long-term morphodynamic model of a tidal embayment, 1997.

Sinha, B., and R. D. Pingree, The principal lunar semidiurnal tide and its harmonics: baseline solutions for m2 and m4 constituents on the North-West European Continental Shelf, *Continental Shelf Research*, *17*(11), 1321–1365, doi:https://doi.org/10.1016/S0278-4343(97)00007-1, 1997.

Soulsby, R., *Dynamics of marine sands*, Thomas Telford Publishing, doi:10.1680/doms.25844, 1997.

Speer, P., and D. Aubrey, A study of non-linear tidal propagation in shallow inlet/estuarine systems Part ii: Theory, *Estuarine, Coastal and Shelf Science*, *21*(2), 207–224, 1985.

Stutz, M. L., and O. H. Pilkey, A Review of Global Barrier Island Distribution, *Journal of Coastal Research*, pp. 15–22, 2001.

The Open University, Chapter 4 - Principles and Processes of Sediment Transport, in *Waves, Tides and Shallow-Water Processes*, edited by The Open University, Open University Oceanography, pp. 96–124, Butterworth-Heinemann, Oxford, doi:https://doi.org/10.1016/B978-008036372-1/50005-2, 1999.

Todeschini, I., M. Toffolon, and M. Tubino, Long-term morphological evolution of funnel-shape tide-dominated estuaries, *Journal of Geophysical Research: Oceans*, *113*(C5), doi:https://doi.org/10.1029/2007JC004094, 2008.

Van de Kreeke, J., Stability of tidal inlets—Pass Cavallo, Texas, *Estuarine, Coastal and Shelf Science*, *21*(1), 33–43, doi:https://doi.org/10.1016/0272-7714(85)90004-6, 1985.

Van de Kreeke, J., Stability analysis of a two-inlet bay system, *Coastal Engineering*, *14*(6), 481–497, doi:https://doi.org/10.1016/0378-3839(90)90031-Q, 1990.

Van de Kreeke, J., and K. Robaczewska, Tide-induced residual transport of coarse sediment; Application to the Ems estuary, *Netherlands Journal of Sea Research*, *31*(3), 209–220, doi:https://doi.org/10.1016/0077-7579(93)90022-K, 1993.

Van der Spek, A. J. F., The development of the tidal basins in the Dutch Wadden Sea until 2100: the impact of accelerated sea-level rise and subsidence on their sediment budget – a synthesis, *Netherlands Journal of Geosciences*, *97*(3), 71–78, doi:10.1017/njg.2018.10, 2018.

Van Goor, M. A., T. J. Zitman, Z. B. Wang, and M. J. F. Stive, Impact of sea-level rise on the morphological equilibrium state of tidal inlets, *Marine Geology*, *202*(3), 211–227, doi:https://doi.org/10.1016/S0025-3227(03)00262-7, 2003.

Van Veen, J., Onderzoekingen in de hoofden in verband met de gesteldheid der Nederlandsche kust, *Rijksuitgeverij Dienst Van De Nederlandsche Staatscourant*, 1936.

Wang, Z. B., E. P. L. Elias, A. J. F. van der Spek, and Q. J. Lodder, Sediment budget and morphological development of the Dutch Wadden Sea: impact of accelerated sea-level rise and subsidence until 2100, *Netherlands Journal of Geosciences*, *97*(3), 183–214, 2018.